Rev.Adv.Mater.Sci. 26(2010) 1-29

SYNTHESIS OF SILVER NANOPARTICLES IN DIELECTRIC MATRIX BY ION IMPLANTATION: A REVIEW

A.L. Stepanov

Laser Zentrum Hannover, 30419 Hannover, Germany
Kazan Federal University, 420018 Kazan, Russian Federation
Kazan Physical-Technical Institute, Russian Academy of Sciences, 420029 Kazan, Russian Federation

Received: February 14, 2010

Abstract. Results on ion-synthesis and optical absorption properties of silver nanoparticles in various dielectrics are reviewed. Composites prepared by the low energy ion implantation are characterized by the growth of metal particles with a size distribution in the depth from the irradiated substrate surface. Such structures lead to specific optical properties of implanted materials, partially to difference in reflection measured form implanted and rear face of samples. The unusual optical absorption of silver nanoparticles fabricated in polymer is also considered. Weak and broad plasmon resonance spectra of the silver nanoparticles are explained in the frame of the carbonization of ion-irradiated polymer. The practical recommendations for fabrication composites with implanted metal nanoparticles for optoelectronics are discussed.

1. INTRODUCTION

At the modern technological time, there is a strong demand to develop new techniques to fabricate and measure the properties of nanomaterials and relevant devices. Significant advancement was made over the last decades in both fronts. It was demonstrated that materials at the nanoscale have unique physical and chemical properties compared to their bulk counterparts and these properties are highly promising for a variety of technological applications. One of the most fascinating and useful aspects of nanomaterials is their optical properties. Applications based on such physical properties of nanomaterials include optical detectors, laser, sensor, imaging, display, solar cell, photocatalysis, photoelectrochemistry and biomedicine [1]. Among variety of nanomaterial a most fascinating ones are composite materials containing metallic nanoparticles (MNPs) which now considered as a basis for designing new photonic media in optoelectronics and nonlinear optics [2]. Simultaneously with the search for and development of novel technologies intended for nanoparticle synthesis, substantial practical attention was devoted to designing techniques for controlling the MNP size and size distribution. This is caused by the fact that the properties of MNPs, such as the quantum size effect, single-electron conduction, *etc*., which are required for various applications, take place up to a certain MNP size. An example of such application in optoelectronics is a prototype of integrated electronic circuit with fibers as guides of optical signals. It is expected that light waveguides used instead of metallic conductors will improve the data rate by at least two orders of magnitude. Moreover, there is good reason to believe that optical guide elements will reduce the energy consumption and heat dissipation, since metallic or semiconductor components of the circuits may be replaced by dielectric ones in this case. Prototype optoelectronic chips currently available are capable of handling data streams with

Corresponding author: A.L. Stepanov, email: aanstep@gmail.com

a rate of 1 Gbit/s, with improvement until 10 Gbit/s in future. Key elements of dielectric waveguides used for light propagation are nonlinear optical switches, which must provide manipulation of laser signal for pulse duration as short as pico- or femtoseconds. The nonlinear optical properties of MNP-containing dielectrics stem most suited from the dependence of their refractive index and nonlinear absorption on incident light intensity [2,3]. Enhanced linear optical absorption in MNPs is called as surface plasmon resonance (SPR). This effect is associated with MNPs, which exhibit an enhancement of local electromagnetic field in a composite and, as consequence, a high value of the third order nonlinear susceptibility when exposed to ultrashort laser pulses [4]. Therefore, such MNP-containing dielectric materials may be used to advantage in integrated optoelectronic devices. In practice, to reach the strong linear absorption of a composite in the SPR spectral region, attempts are made to increase the concentration (filling factor) of MNPs. Systems with a higher filling factor offer a higher nonlinear susceptibility, when all other parameters of composites being the same. Usually noble metals and copper are used to fabricate nonlinear optical materials with high values of third order susceptibility.

There are various ways to synthesize MNPs in dielectrics, such as magnetron sputtering, the convective method, ion exchange, sol–gel deposition, *etc*. One of the most promising fabrication methods is ion implantation [5-10] because it allows reaching a high metal filling factor in an irradiated matrix beyond the equilibrium limit of metal solubility and provides controllable synthesis of MNPs at various depths under the substrate surface. Nearly any metal–dielectric composition may be produced using ion implantation. This method allows for strict control of the doping ion beam position on the sample surface with implant dose as, for example, in the case of electron- and ion-beam lithography. Today, ion implantation is widely used in industrial semiconductor chip fabrication. Therefore, the combination of MNP-containing dielectrics with semiconductor substrates by same technological approach as ion implantation could be reached quite effective.

The history of MNP synthesis in dielectrics by ion implantation dates back to 1973, when a team of researchers at the Lyons University in France [11,12] pioneered this method to create particles of various metals (sodium, calcium, *etc*.) in LiF and MgO ionic crystals. Later, ion-synthesis of noble nanoparticles was firstly done in study of Au- and Ag-irradiated lithia-alumina-silica glasses [13,14]. Developments were expanded from the metal implants to the use of many ions and the active formation of compounds, including metal alloys and totally different composition precipitate inclusions. In ion implantation practice MNPs were fabricated in various materials, such as polymers, glass, artificial crystals, and minerals [15,16]. By implantation, one can produce almost any metal–dielectric composite materials, as follows from Table 1, which gives a comprehensive list of references of various dielectrics with implanted silver nanoparticles with conditions for their fabrications. This review focuses on recent advantages in fabrication of silver nanoparticles by low-energy in implantation in various inorganic matrixes, generally in soda-lime silicate glass (SLSG) and SiO_2. Comprehensive list of publications, which available in scientific literature until 2009 [17-161], Table 1.

2.1. Distribution of implanred silver in the substrate dapth: factor of ion diffusion

The formation of MNPs resulting from ion implantation into dielectric substrates is complex, since there are a large number of factors. A simple ion range estimate of the silver concentration can be computed, but this is only a precursor of processes involving diffusion and clustering and so simple simulations of the entire process are rather challenging. Thus, the process should be divided into subprocesses with a time scale that resolves implantation, diffusion and particle growth. The first step for consideration is the dependence of the implanted ion depth distribution caused by silver diffusion at different substrate temperatures. At simplest consideration, implanted ions during the irradiation lead to a depth distribution in the substrate, which has approximately a Gaussian shape, as described by range algorithms such as TRIM [162]. The diffusion equation of ion-implanted impurities is assumed to be expressed as [163]:

$$\frac{\partial T(x,t)}{\partial t} = D \cdot \frac{\partial^2 N(x,t)}{\partial x^2} + n(n,t), \qquad (1)$$

where *N(x,t)* is the concentration of implanted ions, *D* is their diffusion coefficient, *n(x,t)* is the generation rate of the impurities due to ion implantation, *x* is a distance from irradiated substrate surface and *t* is a duration of implantation. The diffusion coefficient in Eq. (1) is assumed to be independent of the

Table 1. Types of dielectric inorganic matrix with silver nanoparticles synthesized by ion implantation combined in some cases with post-implantation heat treatment. Abbreviations –$2Ag_2O \times 3Na_2O \times 25ZnO \times 70TeO_2$ (ANZT glass), alkali-borosilicate glass (ABSG), borosilicate Pyrex glass (BPYR), soda-lime silicate glass (SLSG), yttria stabilized cubic zirconia (YSZ); optical reflection (OR), optical absorption (OA), transmission electron microscopy (TEM), TEM cross-section (TEM-CS), high resolution TEM (HRTEM), scanning transmission electron microscopy (STEM), conductivity measurements (CM), atom force microscopy (AFM), optical microscopy (OM), R – resistivity, selected area electron diffraction (SAED), energy dispersive X-ray spectrometry (EDS), high-resolution X-ray diffraction (XRD), Z-scan, RZ-scan by reflection,– degenerate four wave mixing (DFWM); room temperature (RT).

Matrix type	Ion energy, keV	Ion dos, ion/cm^2	Current density, μA/sm^2	Matrix temperature °C	Post-implantation heat treatment	Methods of particle detection	Authors
Al_2O_3 crystal <1010>	50 360	4.0×10^{16} 5.0×10^{16} 8.0×10^{16}	1-5	77K 300	Annealing in air at 650 °C, 30 min.	OA	Rahmani *et al.* 1988 [17]1989 [18]
Al_2O_3 crystal <0001>	1.8×10^3	1.2×10^{17}		77K	Annealing in air at 1100 °C, 2 h	OA, DFWM	White *et al.* 1993 [19]
Al_2O_3 crystal	1.5×10^3	8.0×10^{16}	2<		Annealing in air at 500 °C, 1 h	OA	Ila *et al.* 1998 [20]
Al_2O_3 crystal	25 30	$(0.2\text{- }2.0)\times10^{17}$				OA, OR, TEM	Steiner *et al.* 1998 [21]
Al_2O_3 crystal	30	3.8×10^{17}	3, 6, 10	RT		OA RZ-scan	Ganeev *et al.* 2005 [22]2006 [23]
Al_2O_3 crystal	160	$(0.1\text{-}1.0)\times10^{17}$				OA	Marques *et al.* 2006 [24]
ABSG, BPYR glass	270	1.5×10^{16}				OA	Mazzoldi *et al.* 1993 [25]
MgO crystal (100)	180	$(0.5\text{-}1.0)\times10^{17}$	1	RT	Some samples annealed in vacuum at 25-1500 °C	OA TEM	Abouchacra and Serughetti 1986 [26] Fuchs *et al.* 1988 [27]
MgO crystal (100)	1.5×10^3	1.2×10^{17}	2-3	27 C	Annealing in air at 550 and 1100 °C	OA TEM	Qian *et al.* 1997 [28] Zimmerman *et al.* 1997 [29]

MgO crystal (100)	600	1.0×10^{16}		RT	Annealing in air at 1200 °C, 22 h	OA, XRD TEM-CS	van Huis *et al.* 2002 [30]
MgO crystal (100)	200	2.0×10^{17}	2	RT	Some samples annealed in air, Ar, O_2 or 70%N_2 + 30%H_2, at 300-900 °C, 1 h	OA, SAED TEM-CS	Xiao *et al.* 2008 [31]
$MgOP_2O_5$ glass	150	$(0.1\text{-}1.0)\times10^{17}$	0.5-3	RT		OA	Matsunami and Hosono 1993 [32]
Lithia-alumina-silica glass	275-285	1.0×10^{16}	1-2	300		OA	Arnold and Borders 1976 [14]
$LiNbO_3$ crystal	50 360	$(4.0\text{-}0.8)\times10^{16}$	1-4	77K 300	Annealing in air at 250-650 °C, 30 min	OA	Rahmani *et al.* 1988 [17]1989 [18]
$LiNbO_3$ crystal	20, 25 3×10^3 4.2×10^3	$(0.5\text{-}8.0)\times10^{16}$		RT	Some samples annealed in air at 200-600 °C, 1-3 h	OA OM X-ray	Deying *et al.* 1994 [33] Shang *et al.* 1996 [34] Saito and Kitahara 2000 [35] Fujita *et al.* 1994 [36]
$LiNbO_3$ crystal	160 1.5×10^3	2.0×10^{16} 4.0×10^{16} 1.7×10^{17}		RT 500	Some samples annealed in air at 500-800 °C, 1 h	OA Z-scan TEM TEM-CS	Sarkisov *et al.* 1998 [27-40] 1999 [41] 2000 [42] Williams *et al.* 1998 [43, 44] 1999 [45]
$LiNbO_3$ crystal	1.5×10^3	2.0×10^{16}		300	Annealing in Ar gas at 100-1100 °C, 30 min	OA TEM TEM-CS	Amolo *et al.* 2006 [46]
SiO_2 crystal	200	$(2.3\text{-}9.0)\times10^{16}$	1-5	77 300	Annealing in air at 300-500 °C, 30 min	OA	Rahmani and Townsend 1989 [18]
SiO_2	65 130 270	$(1.5\text{-}5.0)\times10^{16}$	1 1.5	300	Some samples annealed in air or 4 % H_2 gas	OA TEM EXAFS	Mazzoldi *et al.* 1993 [47] Mazzoldi *et al.* 2005 [48] Mazzoldi *et al.* 2007 [49] Antonello *et al.* 1998 [50] Battaglin *et al.* 1998 [51] 2001 [52] Bertoncello *et al.* 1998 [53] Caccavale 1998 [54]

							Cattaruzza *et al.* 1999 [55] Gonella *et al.* 1999 [56]
SiO_2	150	$(0.1-6.0)\times10^{17}$	1.5-14	300		TEM-CS, OA	Matsunami and Hosono 1993 [57]
SiO_2	305	$(3.0-9.0)\times10^{16}$	2	0		OA TEM X-ray	Magruder III *et al.* 1995 [58] 1996 [59]2009 [60] Anderson *et al.* 1996 [61] 1997 [62]1998 [63]2000 [64] Zuhr *et al.* 1998 [65]
SiO_2	20-58 130	$(0.4-2.0)\times10^{17}$	0.6	300		AFM	Pham *et al.* 1997 [66]
SiO_2 crystal	200	$(2.3-9.0)\times10^{16}$		300		OA TEM	Liu *et al.* 1998 [67-69]
SiO_2	1.5×10^{3}	2.0×10^{16} 4.0×10^{16} 1.4×10^{17}	2		Annealing in Ar gas at 500-1000 °C, 1 h	OAZ-scan	Ila *et al.* 1998 [70]
SiO_2	65	5.0×10^{16}				X-ray EXAFS	D'Acapito and Zontone 1999 [71]
SiO_2	60	4.0×10^{16}	10	RT		OA, AFM	Stepanov *et al.* 2000 [72]2003 [73]
SiO_2	43 90 150 200 300	$(0.06-2.0)\times10^{17}$	0.8-2.5	300	Some samples annealed in air, Ar, O_2 or 70%N_2 + 30%H_2 at 300-800 °C, 1 h	SAED OA, STEM TEM, EDS HRTEM TEM-CS Z-scan	Jiang *et al.* 2000 [74] Ren *et al.* 2004 [75, 76] 2005 [77-79]2006 [80]2007 [81] 2008 [82]2009 [83] Liu *et al.* 2005 [84] Xiao *et al.* 2006 [85]2007 [86, 87] Wang *et al.* 2007 [88] Wang *et al.* 2008 [89] Zhang *et al.* 2004 [90] Cai *et al.* 2008 [91]2009 [92]
SiO_2 sol-gel film	5-100	$(5.0-6.0)\times10^{16}$	1.5-2.5	330 K		TEM HR-TEM XRD, SAED	Armelao *et al.* 2002 [93]
SiO_2 on Si	10 30 40	$(1.0-5.0)\times10^{15}$ $(1.0-5.0)\times10^{16}$ 1.0×10^{17}	2		Annealing in Ar gas at 500-900 °C, 1 h	OR, OR TEM-CS R, TEM HR-TEM	Ishikawa *et al.* 2002 [94]2009 [95] Tsuji *et al.* 2002 [96, 97] 2003 [98]2004 [99]2005 [100] Arai *et al.* 2003 [101] 2005 [102] 2006 [103]2007 [104, 105]

SiO_2	2.0×10^3	$(0.4\text{-}1.0)\times10^{17}$	2	RT	Some samples annealed in 50%N_2+ 50%H_2 gas or in air at 230-800 °C, 1 h	OA TEM HRTEM	Roiz *et al.* 2004 [106] Oliver *et al.* 2006 [107] Cheang-Wong *et al.* 2007 [108] Peña *et al.* 2007 [109]2009 [110] Reyes-Esqueda *et al.* 2008 [111] 2009 [112] Rodrigues-Iglesias *et al.* 2008 [113] 2009 [114] Rangel-Rojo *et al.* 2009 [115]
SiO_2 on Si	40	0.3×10^{15}		RT	Annealing in vacuum at 550 °C, 20 min	TEM	Romanyuk *et al.* 2006 [116]
SiO_2	60	$(0.3\text{-}1.0)\times10^{17}$	3	RT		OAZ-scan	Takeda *et al.* 2006 [117]
SiO_2	32-40 1.7×10^3 2.4×10^3	$(0.1\text{-}1.0)\times10^{17}$	3-5	RT	Some samples annealed in air at 500 °C, 1 h	OA TEM Z-scan	Joseph *et al.* 2007 [118, 119] Sahu *et al.* 2009 [120]
SiO_2	0.65 1.5 3 keV	$(1.2\text{-}4.7)\times10^{15}$	3-5	RT		OA, OR TEM HRTEM TEM-CS	Carles *et al.* 2009 [121]
SiO_2	200	$(0.1\text{-}2.0)\times10^{17}$	< 2.5			OA, TEM TEM-CS Z-scan	Wang *et al.* 2009 [122, 123]
SiO_2+TiO	305	6.0×10^{16}	7			OA TEM-CS	Magruder III *et al.* 2007 [124]
Si_3N_4	20 130	4.0×10^{16}	0.6	300		AFM	Pham *et al.* 1997 [66]
BPYR glass	270	1.5×10^{16}				OA	Mazzoldi *et al.* 1993 [25]
Soda-lime glass	60	2.0×10^{16} 4.0×10^{16}		300		OR TEM-CS	Nistor *et al.* 1993 [125] Wood *et al.* 1993 [1126]
Soda-lime glass	200	$(0.5\text{-}4.0)\times10^{16}$	0.5-2	RT 77 K		TEM TEM-CS OA	Dubiel *et al.* 1997 [127] 2000 [128]2003 [129]2008 [130] Seifert *et al.* 2009 [131]

Soda-lime glass	200	$(0.5\text{-}4.0)\times10^{16}$	0.5-2	RT 77 K		TEM TEM-CS OA	Stepanov *et al.* 1998 [132] 1999 [133-135]2000 [136-139] 2001 [140-142]2002 [143-146] 2003 [147-149]2004 [150, 151] 2005 [152]2008 [153, 154] 2009 [155]
Ta_2O_5	80-130	6.0×10^{16}	0.6 - 6.4	300		AFM	Pham *et al.* 1997 [66]
TiO_2 crystal	50 65	$(0.3\text{-}1.0)\times10^{17}$	2		Annealing in Ar gas at >400 °C, 1 h	OA TEM-CS	Tsuji *et al.* 2002 [156]2003 [157]
TiO_2 sol-gel films	30 65	$(0.1\text{-}0.5)\times10^{17}$	2	RT	Annealing in Ar gas at 300-600 °C, 1 h	OA	Tsuji *et al.* 2005 [158]2006 [159]
YSZ	20 1.5×10^{3} 3.0×10^{3}	$(0.7\text{-}6.0)\times10^{16}$	2	RT	Some samples annealed in air at 500-1000 °C	OA	Saito *et al.* 2003 [160] Fujita *et al.* 2007 [161]

distance x in the following calculation. D depends on the rate of vacancy formation and the pre-existing concentration of silver particles, which act as trapping sites. Initially the generation rate $n(x,t)$ is believed to be of a Gaussian form [9,163] and is given by

$$n(x,t) = \frac{\Phi}{\Delta R_p (2\pi)^{1/2}} \exp\left[-\frac{1}{2}\left(\frac{x - R_p}{\Delta R_p} \right)^2 \right], \quad (2)$$

where Φ is the dose rate per unit area of impurity ions, R_p is the projected range of an implanted ion, ΔR_p is the projected range straggling.

Let us use, as example, the R_p and ΔR_p corresponding to Ag-implantation into SLSG for different energies calculated by computer TRIM (SRIM) algorithm [162]. The concentration profiles for different implant temperatures of Ag ions in SLSG are given by solution of Eqs. (1) and (2) [164] as

$$N(x,t) = \Phi\sqrt{\frac{2Dt + \Delta R_p^2}{2\pi D^2}}\left(-\frac{\alpha^2}{4Dt - 2\Delta R_p^2} \right) - \Phi\sqrt{\frac{\Delta R_p^2}{2\pi D^2}} \exp\left(\frac{\alpha^2}{2\Delta R_p^2} \right) + \frac{\alpha\Phi}{2D} \times \left(\operatorname{erfc}\frac{\alpha}{\sqrt{4Dt + 2\Delta R_p^2}} - \operatorname{erfc}\frac{\alpha}{\Delta R_p\sqrt{2}} \right), \quad (3)$$

where parameter $\alpha = x - R_p$. As seen from Eq. (3), a value of D, which is dependent on temperature, determines the shape of the concentration profile. For an estimate of the silver diffusion coefficient D_{Ag} in SLSG the Arrhenius equation may be applied with known values of the activation energy 0.69 eV and frequency factor of $5.6\cdot10^{-5}$ cm^2/s [165]. If these coefficients are suggested to be time independent for a fixed temperature, then the results of concentration profile calculations for an applied dose rate of $5.58\cdot10^{13}$ ion/cm^2 and a 360 second duration of implantation, which correspond to a total dose of $2\cdot10^{16}$ ion/cm^2, are presented in Fig. 1.

As seen in the Fig. 1, an increasing the temperature from 20 to 100 °C and, consequently, increasing the Ag diffusion coefficient in the SLSG from $2.88\cdot10^{-17}$ to $2.66\cdot10^{-14}$ cm^2/s, leads to a broadening of the initial Gaussian concentration profile and a reduction of the concentration at the peak of the profile. This decreasing in concentration is most critical for samples implanted at low energy especially. Thus, the accumulation of implanted ions in the SLSG layer is strongly affected by the substrate

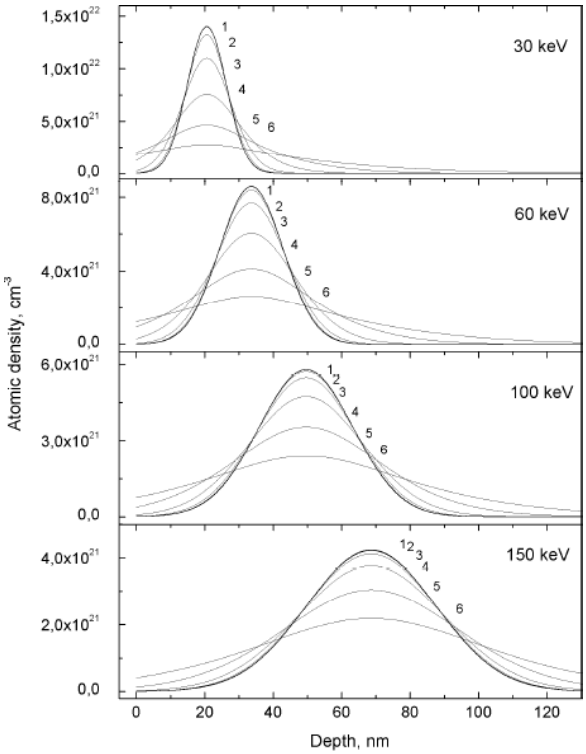

Fig. 1. Calculated ion implanted silver distribution in SLSG as a function of energy, after taking into account the impurity diffusion in dependence on substrate temperature: 1.- TRIM distribution; 2.- 20; 3.-40; 4.- 60; 5.- 80; 6.-100 °C. The concentration profiles correspond to the R_p and ΔR_p of 20.6 and 5.7 nm (30 keV), 33.6 and 9.3 nm (60 keV), 49.6 and 13.8 nm (100 keV), 68.6 and 18.8 nm (150 keV), respectively [134].

temperature, and hence this in turn influences the rate and depth of the development of the conditions for reaching a sufficient impurity concentration for metal particle nucleation and growth. Obviously, if the Ag mobility is rather high, there is no possibility for nanoparticle nucleation during a reasonable implant time. Such an inhibiting effect had been clearly seen in experiments which recorded depth profiles by RBS measurements of the similar type of SLSG implanted with Ag ions at substrate temperatures higher than ~180 °C [166]. Note also that for this calculation (Fig. 1) it is assumed that the bulk glass temperature, and the local temperature within the implanted layer, is the same. In practice the surface will be heated to a higher temperature than the bulk of the glass.

It should be mentioned that Fig. 1 does not include the influence of diffusion limited by the appearance of metal particles in the implanted mate-

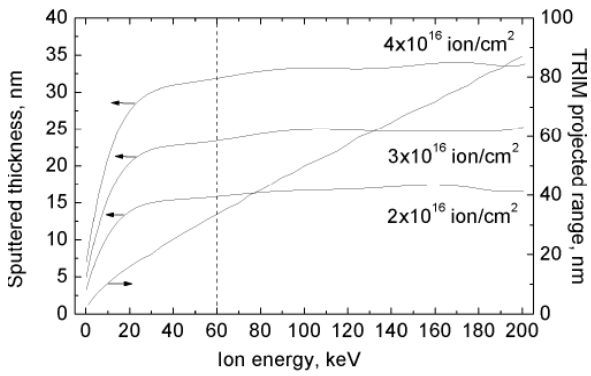

Fig. 2. The calculated dependence of the Gaussian maximum in the depth, excluding sputtering (right hand scale), and thickness of the surface sputtered float glass layer (left hand scale) for Ag implanted into SLSG [167].

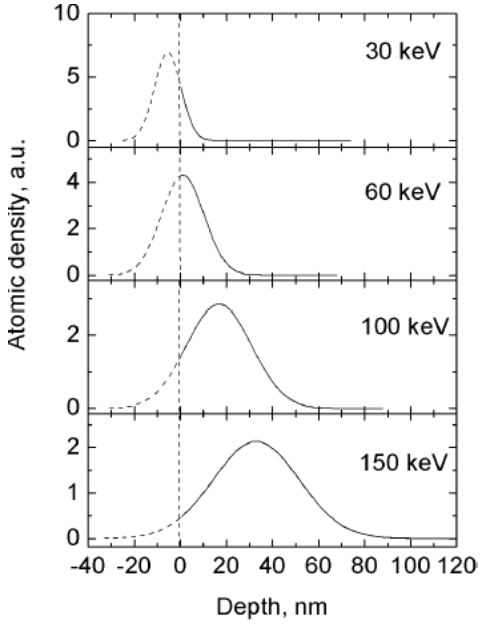

Fig. 3. Calculated ion implanted silver distribution as a function of energy after taking into account the sputtering yield. The vertical dashed line indicates the final surface position, and the left part of the ion distribution from this point shows the sputtered ion portion [167].

rial. However, it was shown, in an example of implantation of Ag ions into SiO_2 glass [57] that the impurity diffusion coefficient drops dramatically after MNP formation, which act as traps for mobile ions. This suggests that the critical time for control of the nanoparticle spacing in the depth and nucleation is at the beginning of the implant, and therefore both the substrate temperature and ion beam currents during this initial phase are also crucial. After MNP formation has commenced, any changes, such as increasing temperature or increases in ion current, will presumably have effects on the particle sizes, but less influence on the depth profile of the distribution. High temperature conditions in the initial stages of implantation will increase the impurity diffusion and so reduce the supersaturation, which is required for particle nucleation. Hence nanoparticles may not form. These conclusions are important as they emphasize that there is a need to control the temperature and ion beam current density throughout the implant. Many experimentalists fail to do a temperature control, but instead allow the temperature to rise from the beam heating. In some cases the initial dose is provided at a low current density in order to avoid surface charging, and hence changes in the ion beam energy. Once some implantation has occurred the surface conductivity is increased and hence the beam currents can be raised. The foregoing conclusions suggest both situations influence the nanoparticle sizes and their depth distributions.

2.2. Distribution of implanred silver in the substrate dapth: factors of irradiation energy and surface sputtering

As was noticed, in first approximation, implantation of ions leads to a depth distribution in the substrate which is approximately Gaussian as described by range algorithms such as TRIM [162]. However, the interaction of implanted ions with the substrate produces also to ejection (sputtering) of ions and neutrals from the surface [9,163]. This sputtering yield is a function of the incoming ion energy, dose and the masses of the ion and target atoms. Figs. 2 and 3 show the calculated thickness of the sputtered layers for SLSG, and the corresponding TRIM concentration profiles of the Ag-ion implantation [167]. In Fig. 3 secondary features such as alterations in range with time dependent compositions after sputtering (and diffusion) was ignored. Nerveless, these figures demonstrate that for 60 keV Ag-implantation the experimental detected depth concentration in the SLSG differs from an assumed Gaussian profile, and in real sample have a maximum concentration curve just near the surface.

To take into account the alterations in range by dose effect changes in composition, new simulations, using a dynamic computer code DYNA [168,169], based on binary collision approximations in intermixed layer formations and sputtering processes, were applied for Ag ion implantation into amorphous insulators: SiO_2, Al_2O_3, and SLSG [137].

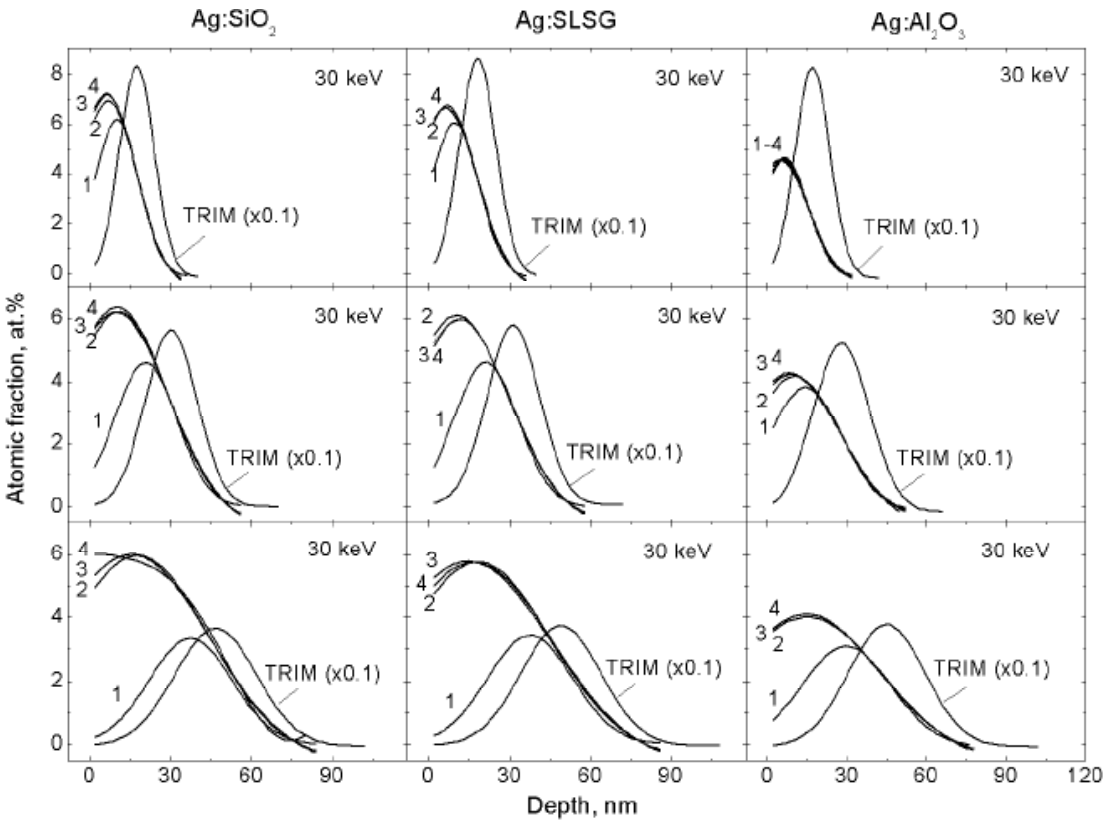

Fig. 4. Calculated Ag-ion implanted depth distributions in amorphous dielectrics: SiO_2, Al_2O_3 and SLSG as a function of energy and dose: 1- 0.1·; 2- 0.3·; 3- 0.6· and 4- $1\cdot10^{16}$ ion/cm^2. There is also a profile corresponding to the TRIM simulations, which does not take into account sputtering and atom-target mixing effects [137].

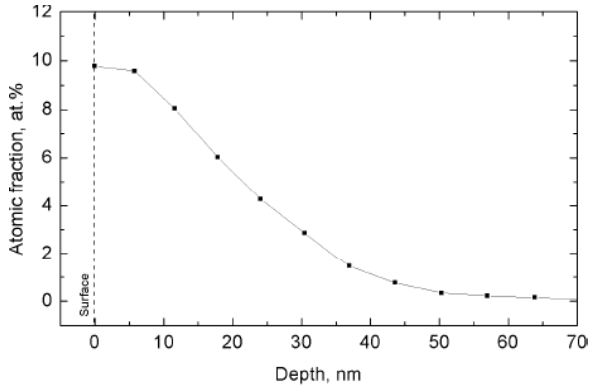

Fig. 5. The depth distribution of silver derived from the RBS spectrum for ion dose of $7\cdot10^{16}$ ion/cm^2 at 60 keV into the SLSG [133].

To include a change of the near-surface layer composition due to cascade atom mixing into a concentration profile calculation, the volume of atoms has to be initially estimated, and was determined here, from the element densities or interatomic separations in the substrates. The sputtering yields at normal ion incidence are dependent on the energy of the metal-ion implantation and were separately calculated using the SRIM-2000 (TRIM) program [162] with the corresponding binding, surface and lattice energies for amorphous SiO_2, Al_2O_3 and SLSG. The elemental concentrations for ion energies of 30, 60, and 100 keV have been obtained at doses of 0.1, 0.3, 0.6, and $1\cdot10^{16}$ ion/cm^2. The dose step in the calculations was $5\cdot10^{14}$ ion/cm^2.

The results of DYNA calculations for Ag ion implantation into different dielectrics are presented in Fig. 4 [137]. Curves marked “TRIM” in these figures correspond to statistical TRIM calculations, which produce the Gaussian impurity distributions. Other curves 1-4 show the DYNA concentration profiles simulated for doses of 0.1, 0.3, 0.6, and $1\cdot10^{16}$ ion/cm^2. As shown here the peak position of the DYNA profiles appear closer to the implanted surface than the symmetrical TRIM curve. Also, the shapes of DYNA curves become asymmetrical, when the dose exceeds a critical value.

In the cases of higher energy (60–100 keV) implantation it is possible to see a dynamic development of the concentration profile during the time of accumulation of implanted ions in the substrates. At the start of the implantation the impurity distribu-

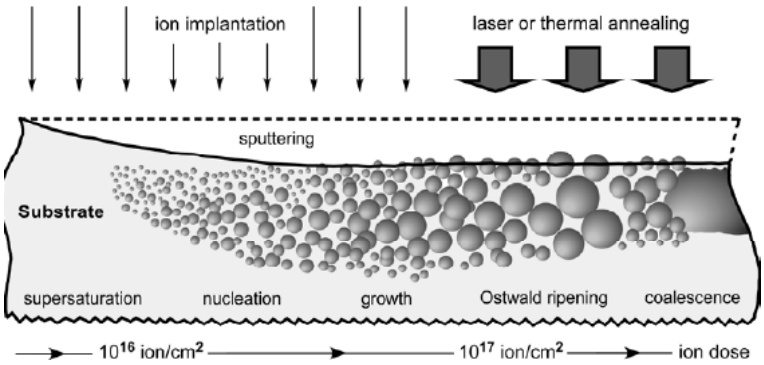

Fig. 6. Basic physical processes (from left to right) involved in the formation of nanoparticle from an implant vs. the ion dose with regard to surface sputtering under irradiation.

tion matches the TRIM curve. As is known, high dose irradiation can, in principle, alter or limit the ultimate concentrations attainable, because of some competition between the sputtering process, and change of both the composition and density of the surface substrate layer by introduction of ions and intermixing with volume atoms. During ion implantation, the sputtering process removes both target and implanted ions. Eventually, an equilibrium condition (steady state) may be reached, where as many implanted atoms are removed by sputtering as are replenished by implantation. The depth distribution of implanted atoms under this condition typically has a maximum at the surface and falls off over a distance comparable to the initial ion range. As seen in Fig. 4 this competition for the case of Ag ion implantation into dielectrics, leads to a shift of the concentration profile to the surface with increasing dose. Thus the profiles become very asymmetrical.

All calculations were obtained at the dose simulations below 10^{16} ion/cm^2, because at higher dose implantation the increasing metal-ion concentration is above the solubility limit in these dielectrics [9]. This causes nucleation and growth of the MNPs that immediately alters the implanted ion penetration depth in the near-surface layer. Though it is impossible to calculate a correct DYNA ion-profile for high doses, nevertheless the metal distribution in implanted insulators for such cases may also be predicted from the present calculated data. Since both the increase of metal concentration in the depth profile and the sputtering yield depend on implantation time, then the metal particle nucleation and growth will also vary with time and depth. It is obvious that during implantation the size and growth of the particles with depth is *"proportional"* to the metal filling factor, because they are both determined by the ion concentration profile. Consequently, in accord with the calculated asymmetrical profiles for a dose of 10^{16} ion/cm^2 Fig. 4, the large MNPs (or/and the higher filling factor) in the same insulators implanted with higher doses will be close to the implanted surface, with small ones in the interior of the implant zone. These predicted features for implanted MNPs are qualitatively confirmed by the silver depth concentration in the SLSG (Fig. 5) derived from experimental Rutherford backscattering (RBS) [133] corresponds to present calculations.

3.1. Ion-synthesis of silver nanoparicles: low energy implantation

Ion implantation is an effective technological tool for introducing single impurities into the surface layer of the substrate to a depth of several micrometers. The degree of surface modification of the materials depends on their individual chemical and structural properties, as well as on variations of implantation parameters, such as the type and energy of an implant, current density in ion beam, substrate temperature, *etc*. A most critical parameter is ion dose F_0, which determines the implant amount. Depending on the modification of dielectrics by irradiation, ion implantation can be conventionally divided into low-dose and high-dose processes.

In the case of low-dose irradiation ($\sim F_0 \leq 5.0 \cdot 10^{14}$ ion/cm^2), the Ag ions implanted, after stopping and thermalization, are dispersed throughout the volume of the dielectrics and are well separated from each other. The energy of the implant is transferred to the matrix via electron shell excitation (ionization) and nuclear collisions. This causes radiation-induced defects, which, in turn, may reversibly or irrevers-

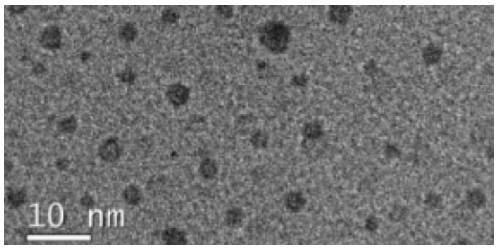

Fig. 7. Plan-view TEM image of SiO_2 with Ag nanoparticles fabricated at a dose of $6.0 \cdot 10^{16}$ ion/cm^2 and an energy of 3 keV. Fragment of an image from [121].

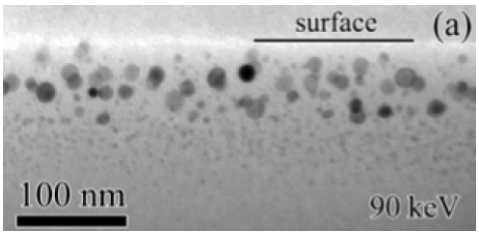

Fig. 8. Cross-section TEM image of SiO_2 with Ag nanoparticles fabricated at a dose of $5.0 \cdot 10^{16}$ ion/cm^2 and an energy of 90 keV. Fragment of an image from [81].

ibly modify the material structure [9]. Various types of crystal structure damage have been observed in practice: extended and point defects, amorphization and local crystallization, precipitation of a new phase made up of host atoms or implanted ions, *etc*.

In the range of high-dose implantation $10^{15} \leq \sim F_0 \leq 10^{16}$ ion/cm^2, the concentration of Ag ions exceeds the solubility limit of metal atoms in matrices and the system relaxes by nucleation and growth growth of MNPs (Fig. 6), as illustrated in plane [121] and cross-section [81] transmission electron microscopy (TEM) views of SiO_2 glass with ion-synthesized Ag particles (Figs. 7 and 8). The threshold dose value (at which MNPs nucleate) depends on the type of the dielectric matrix and implant. For example, for 25-keV Ag^+-ion implantation into $LiNbO_3$, the threshold dose was found to be $F_0 \sim 5.0 \cdot 10^{15}$ ion/cm^2 [33], for 30-keV silver ions embedded in epoxy glassy resin, $F_0 \sim 10^{16}$ ion/cm^2 [170]. The next subrange of high-dose implantation, $\sim F_0 \geq 10^{17}$ ion/cm^2, leads to the coalescence of already existing MNPs with the formation of either MNP aggregates or thin quasi-continuous metallic films near the dielectric surface. For instance, the irradiation of silicone polymer-glass by 30-keV Ag ions at higher-than threshold-nucleation doses favors the formation of aggregate structures (Fig. 9) [171]. The MNP distribution established in the dielectrics after coalescence or Ostwald

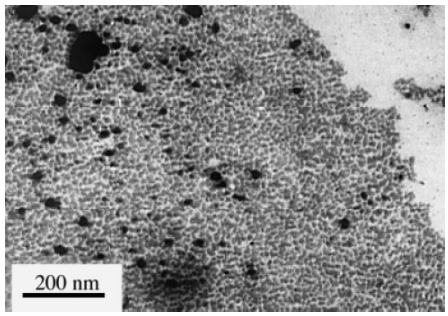

Fig. 9. Plan-view TEM image of silicone polymer-glass with Ag nanoparticles fabricated at a dose of $3.0 \cdot 10^{16}$ ion/cm^2 and an energy of 30 keV [170].

ripening may be dramatically disturbed by postimplantation thermal or laser annealing.

3.2. Ion-synthesis of silver nanoparicles: near room substrate temperature

Although the implantation is made with Ag ions, the dynamics within the ion beam trajectory in the glass and the fact that there is a large capture cross-section for electrons of matrix atoms at low ion velocities, means that the Ag ion in dielectrics will have a high probability of being in a neutral charge state (Ag^0) as it slows down. The mobility of the neutral atom is higher than that of the ion and additionally there are chemical reactions between the silver and the lattice ions. These are particularly difficult to assess in a target material such as multicomponent SLSG as the surface chemistry of this multicomponent glass is even more complicated than within the equilibrium conditions of the bulk material. Analyses of the surface show quite different depth distributions of the host elements, impurities and the tin dopants together with intrinsic structural defects (such as oxygen vacancy sites), and these as well as the dopant ions, exist in several valence states [172]. Within the glass medium there is competition between Ag and other ions for oxygen bond formation. However the differences in Gibbs free energies can lead to Ag-Ag bond formation and hence aggregation of several Ag atoms. As was discussed [173], in spite of the fact that the free energy of silver oxide, at -2.68 kcal/mol at 25 °C, is lower then that for pure metallic silver (0 kcal/mol at 25 °C), the free energy of formation of SiO_2 (~ -200 kcal/mol at 25 °C) is even lower. Consequently there is dissociation of Ag-O bonds to form Si-O and Ag-Ag bonds as this reduces the total energy of the

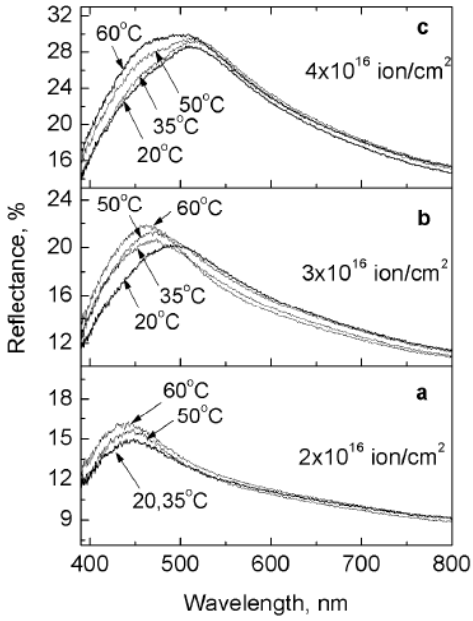

Fig. 10. Reflectance of Ag-implanted SLSG at bulk-substrate temperatures of 20, 35, 50, and 60 °C for various doses [146].

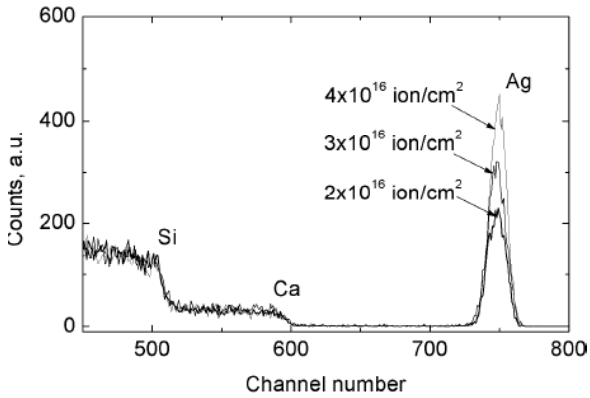

Fig. 11. The RBS data for the Ag-implanted SLSG at a bulk-substrate temperature of 60ºC for various doses [148].

system. These same arguments suggest that the silver nanoparticles have a sharp boundary between the silver and the host glass. However, in some cases there is still evidence, which indicates that an outer silver oxide layer may act as an interface between the glass and the metal.

An excess of neutral Ag atoms in the glass, above the solubility limit, causes nucleation and growth of metal particles. If nucleation and particle growth result from attachment of neutral Ag atoms, then, if slow diffusion of substrate atoms is compared with the rate of incorporation of the implanted impurity species reaching the nucleation sites (diffusion limited growth), the attachment frequency is proportional to both the impurity diffusion coefficient

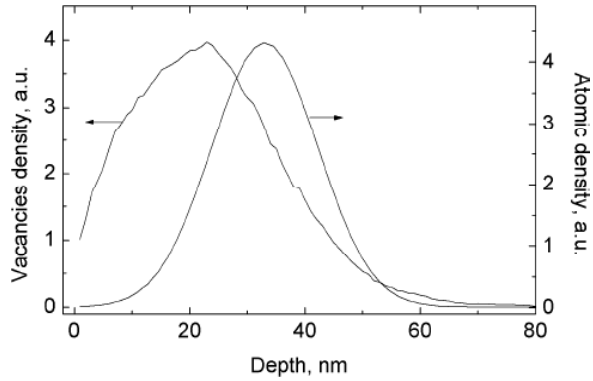

Fig. 12. Calculated 60 keV implanted silver TRIM concentration profile in SLSG (right hand scale), and vacancy distributions (left hand scale), as characteristic of radiation glass damage without taking into account the sputtering process [167].

and to the implant concentration [174]. Since the increase of Ag concentration in the depth profile depends on implantation time, then the MNP nucleation will also vary with time and depth. In such a system the size of the growth particles with depth is partially determined by the ion concentration profile. As was shown above, for present condition of ion implantation the final Ag profile is characterized by a maximum concentration near the surface and differs from the theoretical symmetrical Gaussian distribution of the initial implantation. This implies the larger Ag nanoparticles are close to the implanted glass surface, with smaller particles in the interior of the implant zone. On the other hand, the concentration profile peak of implanted Ag ions moves during implantation, going deeper into the substrate as the sputtering, and hence, the nucleation and growth of metal particles is initiated at different depths, consistent with irradiation time and sputtering.

In practice, optical properties of Ag nanoparticles embedded into glasses are characterised by absorption and reflectance in the visible region. The intensity and spectral position of the peak depends on the concentration and size of the Ag particles, which in the case of spheres, are given by Mie theory predictions at longer wavelengths for large MNP [175], and hence qualitative size estimates may be applied to the optical spectra. In Fig. 10 the optical reflectance of Ag-implanted SLGT corresponding different stages (different doses) of implantation at 60 keV and at various (near-room) temperature of substrate are presented. At an early stage of implantation ($2\cdot10^{16}$ ion/cm^2) the smallest Ag particles appear in the glass at a depth consistent with the

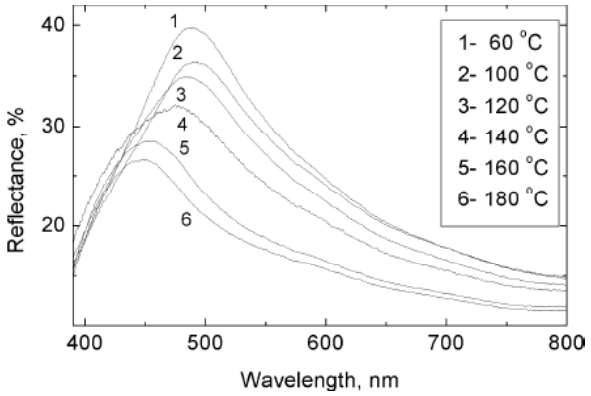

Fig. 13. Reflectance of 60 keV Ag-implanted float glass for a dose of $4 \cdot 10^{16}$ ion/cm^2 at various SLSG temperatures [167].

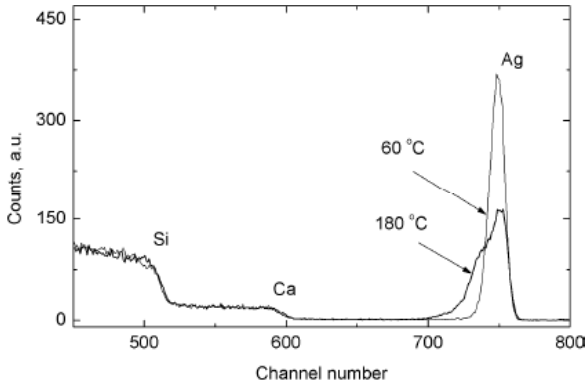

Fig. 14. The RBS data for the 60 keV Ag-implanted float glass for a dose of $4 \cdot 10^{16}$ ion/cm^2 at surface-substrate temperatures of SLSG [167].

Gaussian distribution prediction, and as seen in Fig. 10a, there is no remarkable difference in the reflectance peak positions (~450 nm) between samples prepared at various substrate temperatures (20-60 °C). Increasing the ion dose leads to the appearance of reflectance peaks at different wavelengths and overall changes in the shape of the reflectance in dependence of temperature. For a dose of $3 \cdot 10^{16}$ ion/cm^2 the peaks shifts monotonically to a longer wavelength between 470 nm for a 20 °C and 500 nm for the 60 °C case (Fig. 11b). According analysis with theory Mie, it can be concluded that at higher temperature there are many much smaller MNPs then at 20 °C.

Greater changes in reflectance spectra were registered at the highest dose of $4 \cdot 10^{16}$ ion/cm^2. The samples prepared at temperature higher then 35 °C are characterised by reflectivity consisting of overlapping spectral bands with two maxima, for example at 470 and 510 nm for 50 °C implants as shown by vertical arrows in Fig. 10c, and at least two distinct particle size ranges are favoured. However, in the cases of 20 °C implantation there is evidence of only one broad reflectance peak, also near 510 nm. These differences in reflectance spectra in Fig. 10c, and the corresponding models of the size of the Ag particles, cannot be described by variations in long-range Ag diffusion at 20 to 60 °C (Fig. 1) only, though some differences in diffusion values for these temperatures, of course, essential. The measured RBS data for samples prepared at the highest doses show that the width of the Ag depth penetration is approximately constant (Fig. 11) [134]. Thus the formation of metal particles at high dose appears in the glass layer over the same thickness range for the temperatures between 20 and 60 °C. The explanation of the appearance of a bimodal concentration dependence, which has mainly large particles in the outer region and mostly small particles in the deeper zone, may result because of the variations of the Ag ion concentration into the glass. It was suggested for the case of higher energy (> 150 keV) Ag-implants into glass [32], that one depth region is set by the penetration maximum of the Gaussian concentration profile, and the second is at maximum of glass damage where there are peaks in the vacancy concentration, displaced atoms, pint defects and broken bonds. Similar consideration was applied for the present case of low energy implantation. In Fig. 12 the concentration profile calculated from the TRIM aproach, and the corresponding vacancy profile, are presented for the case of 60 keV Ag implants into SLSG using the SRIM-2000 programme [162]. It is seen that the maximum of glass-damage profile is resolved from the Ag concentration peak, and is placed closer to the irradiated glass surface. Taking into account the enhanced Ag damage-related diffusion to the surface, which is effective at higher temperature (60 °C), it is possible to explain the probabilities for accumulation of Ag atoms with the consequent growth of metal particles in the damage region. It should be noted, that damage profiles move from the irradiated substrate surface, consistent with sputtering. Overall the distributions of the impurity and damage profiles can result in formation of bigger particles close to the glass surface, with a range of smaller particles deeper below the surface.

The optical reflectance spectra for similar samples Ag-implanted at the different temperature of SLSG from 60 to 180 °C is presented in Fig. 13 [167]. The net reflectance and average particle size

both decrease with higher temperature implants. The reflectance peak moves from 490 (60 °C) to 450 nm (180 °C) and the intensity decreases by ~14%. This optical result is consistent with RBS data, which shows that the high temperature implants lower the local concentration, both by inward diffusion and by enhanced sputter losses RBS spectra are plotted in Fig. 14 [167]. These indicate a sharp Ag peak at 60 °C, but by 180 °C, there is loss of Ag from the glass surface (~19%) and Ag in-diffusion from the implanted layer. Thus the average Ag size decreases as seen by the reflectance data. Similar trends were exemplified in earlier RBS measurements [166] using implantation at the temberature from 250 to 600 °C. For high-temperature Ag ion implantation into dielectrics, the diffusion coefficient drops dramatically after MNP formation. This means that the critical time for metal particle nucleation is the beginning of the implantation as it was suggested above from TRIM calculation for different temperatures of substrate, and therefore the substrate temperature during this initial phase. After particle nucleation has commenced, any changes, such as increasing temperature from beam heating or increases in ion current, will not interrupt the growth of metal particles. Conversely, high temperature conditions initially will increase the impurity diffusion and so reduce supersaturation and particle nucleation.

4. OPTICAL REFLECTANCE ION-SYNTHESISED SILVER NANOPARTICLES

Ion implantation gives the possibilities for the synthesis of MNPs in the volume of dielectrics with high values for the metal filling factor that lead to new perspectives for their opto-electronic applications. The optical linear and nonlinear properties of glasses containing implanted nanoparticles have been studied extensively by absorption spectroscopy, by the *z*-scan method or by direct measurements of the third-order optical susceptibility. The interpretation of experimental optical data is usually based on a restricted approximation in which the composite material acts as a dielectric medium containing equal-size MNPs, uniformly distributed in the total implanted volume. Moreover many authors assume that the absorption band is defined by measurements of transmission data only, which is incorrect [176]. To derive the absorption properties of a thin composite layer, one must separate effects of absorption from reflection in the measured transmission data. In a simplistic model of a uniform nanoparticle distribution throughout the bulk, there is no inconsistency, but this does not apply to the real ion-implanted material. One of the main features of the ion implantation process is a non-uniform statistical penetration of accelerated ions into the substrate that leads to the growth of MNP with a wide size distribution in the depth from the irradiated glass surface, as was shown by electron microscopy [57,125]. Failure to include this non-uniformity causes considerable error in assessing the particle size distribution and in interpretation of optical properties. One of the possibilities for analysing of optical properties of dielectrics with non-uniform size distribution of refractive index over the depth, is the consideration of the composite as consisting of a number of thin separated layers with specific-size particles [176]. This approach could be also used for modelling and description of the optical reflectance of glass

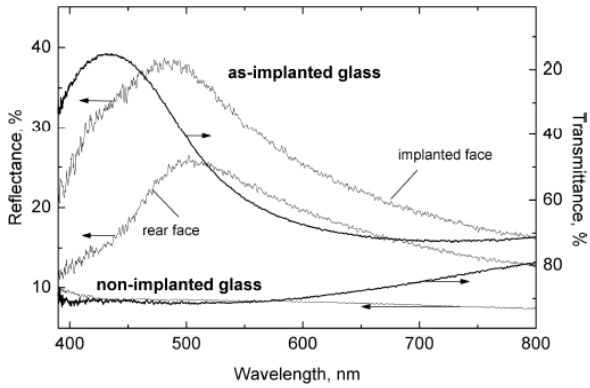

Fig. 15. Optical transmittance and reflectance of the silver implanted SLSG and virgin glass with a dose of $7 \cdot 10^{16}$ ion/cm^2 and an energy of 60 keV. Reflectance was measured from both the implanted and rear faces of the sample [132].

Optical spectra of such implanted glass are presented in Fig. 15. The transmittance spectrum is characterised by a deep minimum near 430 nm and the shape of spectral curve is almost symmetrical. The reflectance spectra are more complex and, although the transmission is the same whether the glass is viewed from the implanted or the reverse face, the shapes of the reflectivity curves differ. Overlapping peaks of reflectance spectra measured from the implant face of the samples exhibit a shoulder at about 430 nm, on the left side of a clearly determined maximum at 490 nm, whereas reflectivity from the rear face appears to have a simpler peak at longer wavelengths near 500 nm.

As the typical sizes of spherical MNPs formed by ion implantation are orders of magnitude smaller

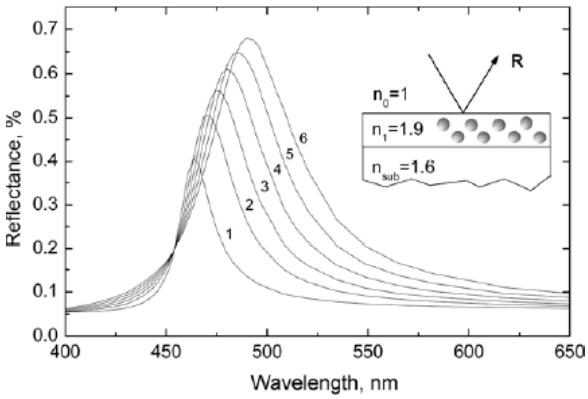

Fig. 16. Calculated optical reflectance of the silver-glass composites. Spectral curves correspond to layers with a metal filling factor: (1) 0.05 , (2) 0.08 , (3) 0.1 , (4) 0.12 , (5) 0.14 , (6) 0.16 [136].

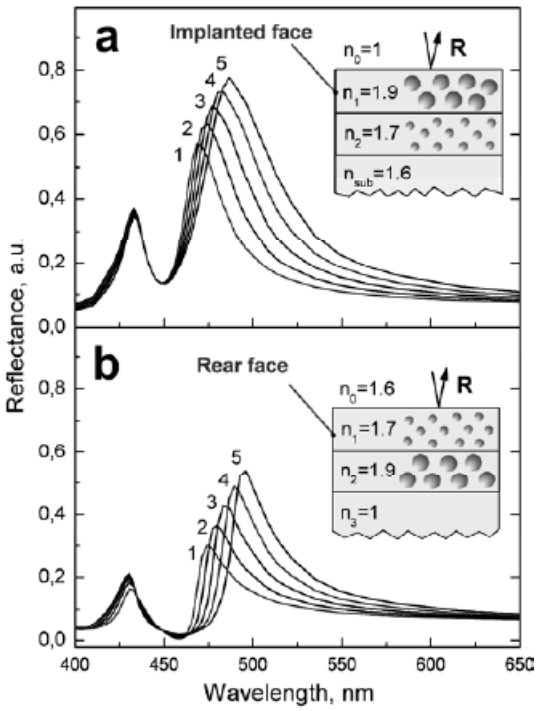

Fig. 17. Calculated optical reflectance of the silver-glass composites. Spectral curves correspond to a layer a with refractive index of 1.9 and a metal filling factor: (1) 0.08 , (2) 0.1 , (3) 0.12 , (4) 0.14 , (5) 0.16. In the layer with refractive index of 1.7 the filling factor is 0.05. Figs. (a) and (b) correspond to implanted and rear face reflectivity, respectively [136].

than the wavelengths of visible light [9] (Figs. 7-9), composite optical properties can be treated in terms of an effective medium theory. Additionaly, the laws of geometric optics for light beam directions and the Fresnel formulae for the intensities can be applied. An effective dielectric permeability, ε_{eff}, provided for dispersions of spherical metal particles with complex dielectric constants, $\varepsilon_{Ag,}$ and a filling factor, *f*, in a surrounding glass (ε_m) for implanted composite may be derived from the effective medium theory, for example Maxwell-Garnet equation [177,178]. For reflectivity evaluation of the composite material with a metal distribution which is changing in depth, and hence with a changing ε_{eff}, the implanted sample was considered as consisting of thin homogeneous isotropic layers characterised with their own constant ε_{eff} and *f*. For calculation of the multilayer reflectance, a matrix method [176] using the complex Fresnel coefficients was applied in this study for the case of normal incidence of the light. The values of *f* and thicknesses of composite layers may be estimated at different depths in the sample from Fig. 5. Assuming the surrounding glass to be a non-absorbing medium it should be noted that the refractive index of SLSG (1.54) increases after incorporation of dispersed silver ions in its volume [179].

Firstly, the case of reflectivity from a single absorbing layer with ε_{eff} on a transparent substrate is considered. Using the symbolic expressions derived from the matrix method for reflectance of such a structure [176], it is possible to calculate the optical spectra of the surface layer. For trial values of: a refractive index (n_1 = 1.9) of the layer containing MNP, thickness of 9 nm, *f* from 0.05 to 0.16 and a refractive index of SLSG substrate with silver atoms as n_{sub} = 1.6, the set of computed spectra are presented in Fig. 16. The reflectance intensity increases and the position of the reflectivity peak shifts continuously toward longer wavelengths with increasing *f*, as expected for optical spectral bands when using the Maxwell-Garnet theory. There is a single maximum corresponding to each *f* value. Hence such a consideration cannot describe the experimental reflectance spectra with at least two overlapping peaks shown in Fig. 15, and modelling in terms of a single-layer structure with an average metal concentration (*f*) is not suitable. Proceeding to the next modelling case of two absorbing layers, each with a thickness of 9 nm on a transparent substrate, generates data of the form shown in Fig. 17. Examples shown in Fig. 17a are modelled for the case of reflectance from the implanted face of an implanted sample where the top medium has a very low refractive index (n_0 = 1), a high index first metal layer with refractive index of n_1 = 1.9, and a second layer with n_2 = 1.7. The value of the substrate refractive index

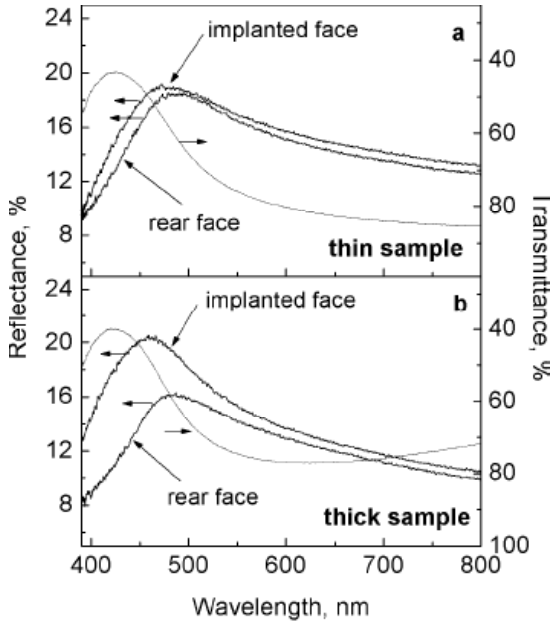

Fig. 18. Comparison of the transmission (right hand scale) and reflectance (left hand scale) of 60 keV Ag-implanted SLSG with dose of $3{\cdot}10^{16}$ ion/cm^2 and at bulk-substrate (target holder) temperatures of 35 °C for various thicknesses of irradiated substrate: a.- this sample of 0.15 mm; b.- thick sample of 3.1 mm. All the samples were measured from the implanted and rear faces [142].

was the same as in the previous system at n_{sub} = 1.6. Optical spectra in Fig. 17a present the calculations when *f* in the surface layer is changed from 0.08 to 0.16, and the deeper layer has a constant *f*=0.05. In Fig. 17a all the examples predict reflectivity from the implanted sample face to be characterised by two peaks: one at 430 nm and another between 440 and 480 nm. The second peak corresponds to the surface layer, where the increasing silver concentration (*f*) shifts the peak position towards longer wavelengths. However, there are clear differences between the experimental reflectivity spectra from the implanted and the rear faces of the layers (Fig. 15), and so calculated spectra for reflectivity from the substrate side of the same multilayer structure are presented in Fig. 17b. Again there are two wavelength peaks, at somewhat different positions in the spectra, and the more intense reflectance band corresponds to the deeper layer, (from this viewing direction). Although the layer with a low value of *f* is effectively the outer layer, for rear face reflectivity, the intensity of the reflectance band at 430 nm corresponding to this layer is weaker than the reflectance for the same layer when measured from the implanted face (Fig. 17a). The second essential feature is that the spectral peaks of the layers with high values of *f* appear at longer wavelengths for reflectance measured from the rear face. This calculation therefore predicts the pattern seen in the experimental reflectance data shown in Fig. 15, that emphasises the differences between front and rear face reflectivity for non-uniform nanoparticle depth distributions and underlines the problem that simple analyses of the transmission and front face reflectivity data do not give all the information required to derive the optical absorption band shapes.

5. INFLUENCE OF SUBSTRATE SURFACE TEMPERATURE ON SYNTHESIS OF SILVER NANOPARTICLES

Inevitably during ion implantation into an dielectrics, which is a poor thermal conductor, there is temperature gradient near the glass surface, as a nucleation and growth in the surface layer differ from those estimated by knowledge of the result of ion beam heating. Hence the effective temperature conditions for metal controlled substrate/holder temperature – bulk glass temperature. The measured parameter is therefore only a first step in the control process, although it can result in reproducible samples. To reveal the influence of the surface temperature gradient on the formation of metal nanoparticles in the glass implantation of thin (0.15 mm) and thick (3.1 mm) SLSG samples at the same temperature of 35 °C were compared [142]. Both samples were fixed to watercooled sample holed during implantation by thermoglue. It was assumed the surface temperature of the thick sample should be higher than in the thinner one and hence identical implant conditions will result in appearance of differences in the size of Ag nanoparticles, and their optical characteristics. Measurements of the transmittance and reflectance from both the implanted and rear face of the samples were made, and corresponding spectra are presented in Fig. 18. As seen from the figure there are no remarkable spectral differences between the transmittance curves from Ag nanoparticles into the samples near 425 nm, but some minor changes in the near-red transmittance. However, there are clear differences in the reflectance data. In previous paragraph the contrast between the information available from transmission and reflectivity has been stressed, and the changes are recognized as coming from the growth of Ag-implanted nanoparticles, which vary with depth into the glass surface.

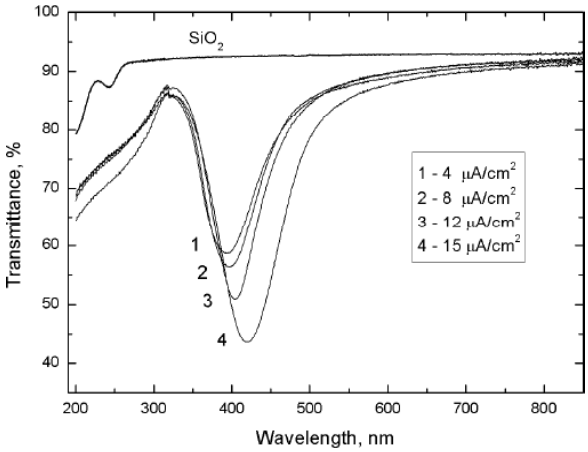

Fig. 19. Transmittance spectra of SiO_2 samples after Ag^+ ion implantation with dose of $5 \cdot 10^{16}$ ion/cm^2 at various ion current densities [151].

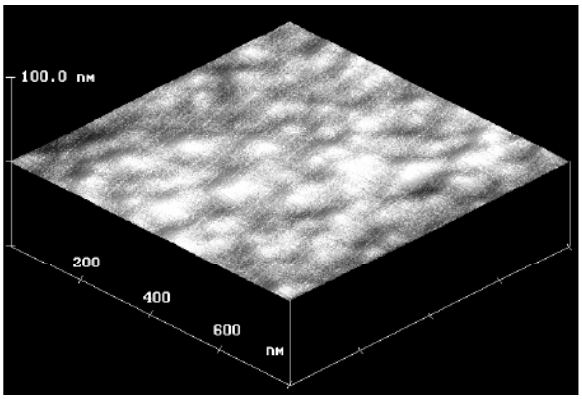

Fig. 20. AFM image of SiO_2 surface before ion implantation [151].

The differences between implanted and rear face reflectivity of a thick sample, which contain peaks near 450 and 475 nm, (Fig. 18b), immediately emphasise that the distribution of particle sizes vary with depth beneath the implant surface. Although the transmission is the same whether the glass is viewed from the implanted or the reverse face, the shapes of the reflectivity curves differ. Whilst the reflectance differences from implanted and rear faces are monitoring an asymmetry of the nanoparticle size distribution and concentration of the particles with depth into the sample, the precise distributions cannot be determined. As already mentioned, particles of larger size are concentrated near the implanted glass surface, whereas small ones occur throughout the ion range. The reflectances from thin and thick samples are very different in spectral shape, although the RBS data for samples in both cases show an approximately constant width for the Ag distribution profile. Moreover, the reflectance from implanted and rear faces of thin samples, with peaks near 470 and 480 nm, are very similar in shape and intensity to each other (Fig. 18a). This suggests that the smaller temperature gradient across the glass results in a more symmetrical particle size distribution with depth. Moreover, the position of reflectance peaks of the thin sample are at longer wavelengths than in thick samples, indicating formation of a more uniform distribution of large particles.

Quite clearly the reason for differences in reflectance between thick and thin samples results from the different temperature gradient at the irradiated surface, and as seen from data in Fig. 18 suggests that for thin samples there is closer control to the base temperature of 35 °C. For thin samples a more uniform particle size-depth distribution was produced than for thick glass targets. Since such temperature gradients and average temperature differences exist relatively close to room temperature, it is worth noting that this is contrary to some of the early models for describing the nanoparticle formation in insulators by ion implantation which are based on thermal spike considerations, as these assume the local temperature inside an ion trajectory within a silicate glass to be ~3,000K [180]. Such mechanisms would not respond in the way described here. Modeling suggests that radiation damage enhanced Ag diffusion in glass is important, as are the temperature gradients, which develop in the surface of the insulator during implantation. Overall the initial beam and temperature conditions have a major influence on the resulting nanoparticle generation.

6. SYNTHESIS OF SILVER NANOPARTICLES IN DEPENDENCE ON ION CURRENT DENSITIES

The fabrication of silver nanoparticles in a dielectric matrix by ion implantation is a complex process which depends on a number of factors. The conditions of metal nanoparticle synthesis can be varied depending on the ion implantation parameters such as ion energy, dose, ion current, target temperature *etc*. In previous paragraphs it was that temperature of the irradiated glass is a significant factor for size control of the MNPs. Unfortunately, the target temperature is often ignored in experiments. Hear consider an influence of the ion current density and concomitant thermal effects on the silver

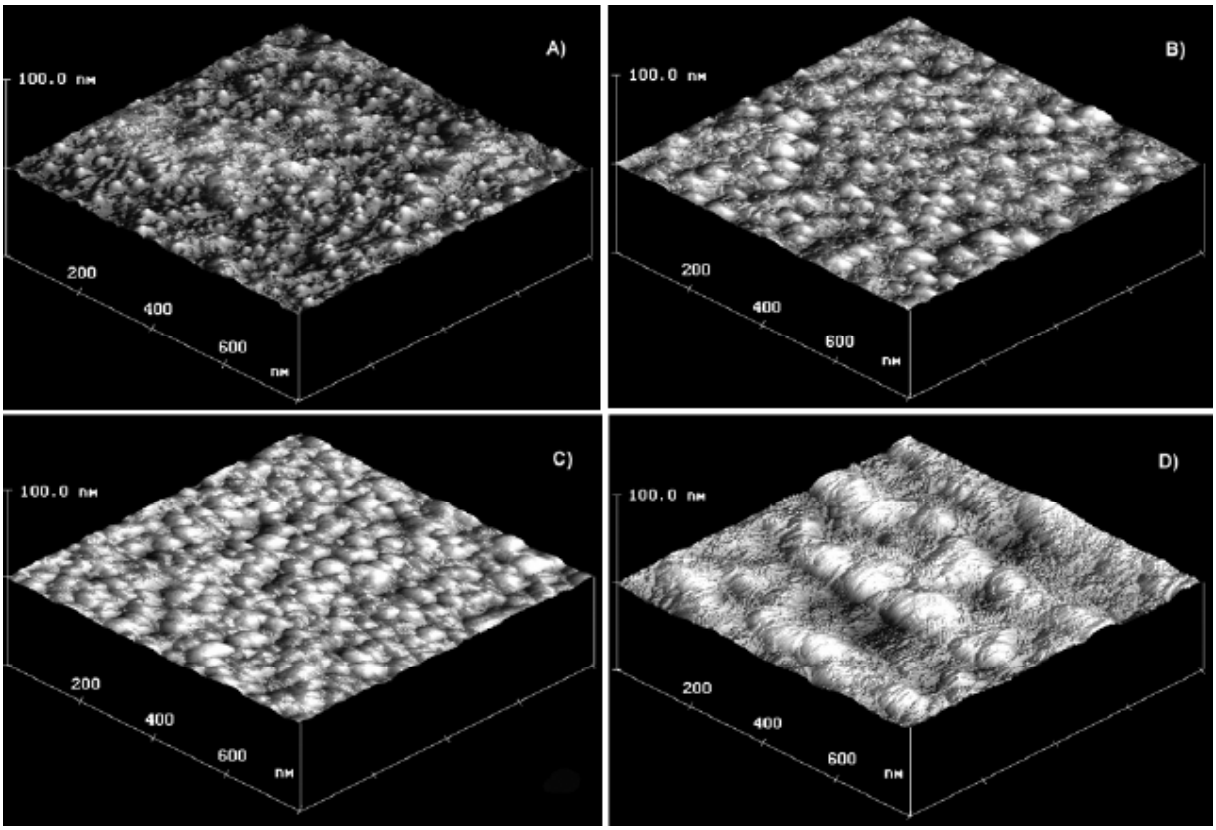

Fig. 21. AFM images of SiO_2 surfaces implanted at different ion current densities: a) 4; b) 8; c) 12; d) 15 $\mu A/cm^2$ [151].

nanoparticle formation and surface modification under the low-energy ion implantation of silicate glass (SiO_2).

Formation of the Ag nanoparticles in the implanted SiO_2 was estimated by the optical transmittance measurements showing an appearance of the characteristic band of SPR absorption. It was observed [151] that the increase of the ion current density monotonically shifts the absorption band to longer wavelengths indicating the rise of the nanoparticle sizes (Fig. 19). AFM image of the virgin glass surface, which is relatively smooth, is shown in Fig. 20. AFM images in Fig. 21 show the glass surface morphology produced by the Ag^+ ion implantation at different current densities in the beam [151]. Compared to Fig. 20, formation of semi-spherical hillocks is observed for all implanted samples. This surface structure is explained by the sputtering of glass layer resulted in partial towering of the spherical-shaped metal nanoparticles nucleated in the near-surface layer of the substrate. Similar morphology was earlier detected by AFM for different metal nanoparticles synthesised in various dielectrics by low-energy implantation, for example: Ag ions into Ta_2O_5, SiO_2, Si_3N_4 [21,66]. It is seen from the images of Fig. 21 that the hillock size (or particle sizes) increases with the ion current density.

The formation of bigger particles at higher ion current densities, when the dose is constant, may be explained by an increase in Ag atom mobility and faster particle nucleation. The increase in the diffusion mobility is expected due to the substrate heating by the implantation at high dose rate. The numerical estimation presented in shown that the coefficient of diffusion of silver atoms in the glass increased for two orders of magnitude with the substrate temperature rise from 20 to 100 °C (Fig. 1). At the beginning of implantation all samples in our case were at the same room temperature but, it is obvious, that by the moment of collection of the ion dose the substrate implanted at higher ion current density has higher temperature. Thus, the change in ion current density under implantation of metal ions into dielectric considerably affects the formation of MNPs. This method can be used for control of particle size to synthesise the metal/dielectric composites with desirable parameters.

Table 2. Types of organic matrix with silver nanoparticles synthesized by ion implantation. (Abbreviations – Polycarbonate (PC), Poly(ethyleneterephthalate (PET), Polyimide (PI), Polymethylmethacrylate (PMMA); Phenylmethyl-silane resin with tin diethyldicaprilate (Silicone resin); optical absorption (OA), transmission electron microscopy (TEM), conductivity measurements (CM); room temperature (RT).

Matrix type	Ion energy, keV	Ion dos, ion/cm^2	Current density, μA/sm^2 °C	Matrix temperature detection	Methods of particle	Authors
Epoxy	30	$(0.1\text{-}1.8)\times10^{17}$	4	RT	OA, TEM	Stepanov *et al.* 1995 [185] 1997 [186]2009 [187] Khaibullin I. *et al.* 1997 [188]
PC	60	3.0×10^{17}	3	-	OA, TEM	Boldyryeva *et al.* 2004 [189]
PET	40	$(0.1\text{-}2.0)\times10^{17}$	4.5	-	CM, TEM	Wu *et al.* 2000 [190] 2001 [191, 192]2002 [193]
PI	130	$(0.1\text{-}5.0)\times10^{17}$	1-3	< 350	TEM	Kobayashi *et al.* 2001 [194]
PMMA	30	$(0.1\text{-}7.5)\times10^{16}$	4	RT	OA, TEM	Stepanov *et al.* 1994 [184] 2000 [195] 2002 [196]2004 [197] Bazarov *et al.* 1995 [198]
PMMA	60	$(0.1\text{-}3.0)\times10^{17}$	3	-	OA, TEM	Boldyryeva *et al.* 2005 [199]
Silicone resin	30	$(0.1\text{-}1.8)\times10^{17}$	4	RT	OA, TEM	Khaibullin R. *et al.* 1998 [200] 1999 [201] Stepanov *et al.* 1995 [202]

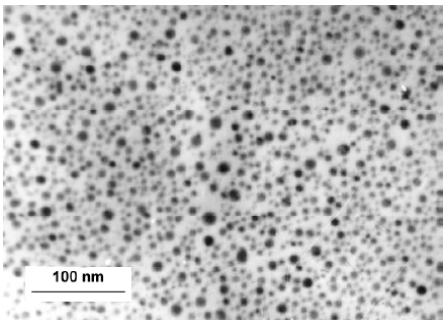

Fig. 22. TEM image of silver nanoparticles fabricated in PMMA by Ag-ion implantation [15].

7. ION SYNTHESIS OF SILVER NANOPARTICLES IN POLYMER MATRIX

The task of designing new polymer-based composite materials containing MNPs is of current interest. nanoparticles may be embedded in a polymer matrix in a variety of ways. These are such techniques as chemical synthesis in an organic solvent [1], vacuum deposition on viscous polymers [181], plasma polymerization combined with metal evaporation [182], *etc*. However, they all suffer from disadvantages, such as a low filling factor or a large distribution in size and shape of nanoparticles, which offsets the good optical properties of composites. Ion implantation is a promising method. Despite the intensive study of MNP synthesis by ion implantation in dielectrics, such as non-organic glasses and crystals, the formation of nanoparticles in organic matrices was realized only at the beginning of the eighties by Koon *et al*. in their experiments on implantation of Fe ions into some polymers in 1984 [183]. A first publication on ion-synthesis of noble metal nanoparticles in polymer was realised in 1995 when silver particles were created in PMMA [184]. In Table 2 a full list of publications on ion synthesis of silver nanoparticles [184-202] with detail implantation conditions is presented. It should be mention that a comprehancive information of nanoparticles of all kind metals ion synthesised in polymer is reviweved in [15].

The aim of this paragraph is to observe the SPR-related optical absorption of silver nanoparticles fabricated in polymethylmethacrylate (PMMA) by implantation with 30 keV Ag^+ ions at doses in the range from $3.1\cdot10^{15}$ to $7.5\cdot10^{16}$ ion/cm^2. Optical spectra of spherical MNPs embedded in various dielectric media can be simulated in terms of the Mie electromagnetic theory [175], which allows one to estimate the extinction cross section s_{ext} for a light wave incident on a particle. This value is related to the intensity loss ΔI_{ext} of an incident light beam I_0 passes through a transparent particle-containing dielectric medium due to absorption σ_{abs} and elastic scattering σ_{sca}, where $\sigma_{ext} = \sigma_{abs} + \sigma_{sca}$. Following the Lambert-Beer law

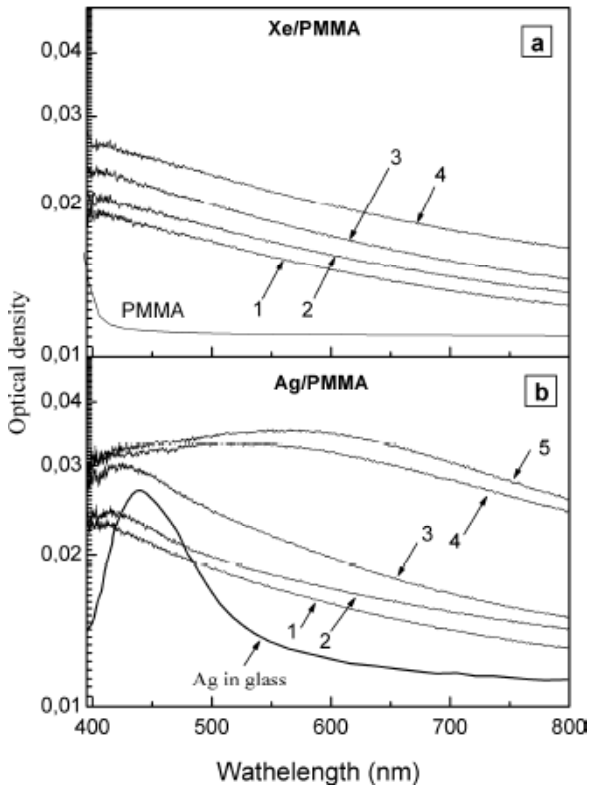

Fig. 23. Optical density spectra from PMMA irradiated by (a) xenon and (b) silver ions for doses of (1) $0.3\cdot10^{16}$, (2) $0.6\cdot10^{16}$, (3) $2.5\cdot10^{16}$, (4) $5.0\cdot10^{16}$, and (5) $7.5\cdot10^{16}$ ion/cm^2. The spectrum taken of SiO_2 implanted by silver ions ($5.0\cdot10^{16}$ ion/cm^2) [195].

$$\Delta I_{ext} = I_0\left(1 - e^{-\#\sigma exth}\right), \tag{4}$$

where h is the thickness of the optical layer and # - the density of nanoparticles in a sample. The extinction cross section is connected to the extinction constant γ as $\gamma = \#\sigma_{ext}$. Experimental spectral dependencies of optical density (*OD*) are given by

$$OD = -\lg\left(I / I_0\right) = \gamma \cdot \lg\left(e\right) h, \tag{5}$$

hence, for samples with electromagnetically non-interacting nanoparticles, it possible to put $OD \sim \sigma_{ext}$. Therefore, experimental *OD* spectra can be compared with modeled spectral dependences that are expressed through σ_{ext} calculated by the Mie theory.

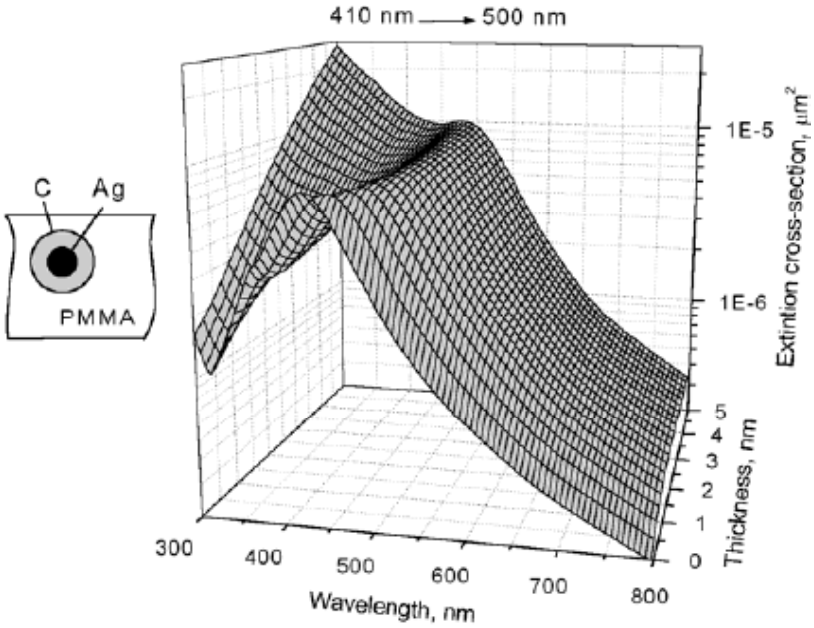

Fig. 24. Simulated optical extinction spectra for 4-nm silver nanoparticles with the carbon shell that are placed in the PMMA matrix vs. sheath thickness [15].

As follows from TEM, Ag-ion implantation results in the formation of silver nanoparticles. As example, the micrograph in Fig. 22 shows spherical nanoparticles synthesized in PMMA at a dose of $5.0 \cdot 10^{16}$ ion/cm^2 [195]. Microdiffraction patterns of the composite samples demonstrate that the MNPs have the fcc structure of metallic silver. The diffraction image consists of very thin rings (corresponding to polycrystalline nanoparticles) imposed on wide diffuse faint rings from the amorphous polymer matrix. By comparing the Experimental diffraction patterns show that implantation does not form any chemical compounds involving silver ions.

Optical absorption spectra of PMMA irradiated by xenon and silver ions at various doses are shown in Fig. 23 [195]. As seen in Fig. 23a, when the xenon ion dose increases, the absorption of the polymer in the visible (especially in the close-to-UV) range also increases monotonically. This indicates the presence of radiation-induced structure defects in the PMMA. The implantation by silver ions not only generates radiation defects but also causes the nucleation and growth of MNPs. Therefore, along with the absorption intensity variation as in Fig. 23a, a selected absorption band associated with silver nanoparticles is observed (Fig. 23b). For the lowest ion dose, the maximum of this band is near 420 nm and shifts to red spectral area (up to ~600 nm) with dose increasing, simultaneously with the band broadening. The maximum of this band is not sharp, although it is definitely related to the SPR effect in the silver nanoparticles. Such broad SPR absorption is untypical for silver nanoparticles in PMMA. When silver particles were synthesized in PMMA by the convection melting technique [203], the SPR band was very sharp, unlike present experiment. Fig. 23 shows the *OD* spectrum for inorganic silica glass irradiated by silver ions under the implantation conditions as here. Particle size distributions in the SiO_2 and PMMA are nearly the same. SiO_2 has the refractive index close to that of PMMA. However, the absorption of Ag nanoparticles in the glass (Fig. 23b) is much more narrow and intense than the absorption of the MNPs in the polymer.

The attenuation (extinction) of an optical wave propagating in a medium with MNPs depends on the SPR absorption and the light scattering efficiency. The wavelength of optical radiation, the particle size, and the properties of the environment are governing factors in this process. Within the framework of classical electrodynamics (the Maxwell equations), the problem of interaction between a plane electromagnetic wave and a single spherical particle was exactly solved in terms of optical constants of the selected materials by Mie [175]. Moreover, to explain the experimental dependences corresponding to high-dose silver implantation into PMMA, it should be consider a difference between implantation into polymers and inorganic materials (silicate glasses, crystals, *etc.*). The most impor-

tant distinction is that, as the dose increases, so does the number of dangling chemical bonds of polymer along the track of an accelerated ions. Because of this, gaseous hydrogen, low-molecular hydrocarbons (e.g., acetylene), CO, and CO_2 evolve from the matrix [204]. In particular, ion-irradiated PMMA loses HCOOCH3 methoxy groups [205]. The evolution of several organic fractions leads to the accumulation of carbon in the irradiated polymer layer, and radiation-induced chemical processes may cause chain linking. Eventually, an amorphous hydrogenated carbon layer is produced.

As was observed [15], extinction spectra for nanoparticles represented as a silver core covered by a carbon shell in an insulating matrix (PMMA) can be well analyzed in terms of the Mie relationships for shelled cores [207]. Modeled optical extinction spectra for a Ag nanoparticle with a fixed size of the core (4 nm) and a varying thickness of the carbon shell (from 0 to 5 nm) are shown in Fig. 23. Simultaneously, the SPR band intensity decreases, while the UV absorption increases, so that the absorption intensity at 300 nm and a shell thickness of 5 nm exceeds the SPR absorption of the particles. Both effects (namely, the shift of the SPR band to longer wavelengths and the increased absorption in the near ultraviolet) agree qualitatively with the variation of the experimental *OD* spectra (Fig. 23b) esspesialy when the implantation dose exceeds $2.5 \cdot 10^{16}$ ion/cm^2. Thus, the assumption [15] that the increase in the carbonized phase fraction with implantation dose and the variation of the *OD* spectra go in parallel is sustained by the simulation of the extinction for complex particles (Fig. 24).

When analyzing the optical properties of nanoparticles embedded in a medium, it should be taking into account effects arising at the particle–matrix interface, such as the static and dynamic redistributions of charges between electronic states in the particles and the environment in view of their chemical constitution. Consider first the charge static redistribution. If an atom is deposited (adsorbed) on the MNP surface, the energy levels of this atom change his positions compared with this in the free state [208].When the number of the adsorbed matrix atoms becomes significant, their contact generates a wide distribution of density of states. Additionally, the adsorbed atoms are separated from surface atoms of the metal by a tunnel barrier. The gap between the energy positions of the adsorbed atoms and the Fermi level of the particles depends on the type of the adsorbate. The overlap between the energy positions of the matrix atoms and the energy positions of the silver surface atoms depends on the rate with which the electrons tunnel through the barrier. Accordingly, the conduction electron density in the particles embedded will change compared with that in the particles placed in a vacuum (without adsorbates): it decreases if the electrons tunnel toward the adsorbed atoms or increases when the electrons tunnel in the reverse direction. Eventually, equilibrium between the particle and the matrix sets in; *i.e.*, a constant electrical charge (Coulomb barrier) forms at the nanoparticle surface.

Such a charge static redistribution due to the deposition of an adsorbate on the particle surface and the respective change in the electron concentration in the MNPs could also observed in the SPR absorption spectra [4]. The incorporation of Ag nanoparticles into the carbon matrix of C_{60} fullerene (or the deposition of carbon on the nanoparticle surface) reduces the concentration of 5*sp* electrons in the particle roughly by 20%, since they are trapped by matrix molecules [208]. It was shown that the decrease of electrons shifts the MNP extinction spectrum toward longer wavelength. This shift of the SPR extinction band to the longer wavelength with increasing of implantation dose in present experiment (Fig. 23) may also be explained by the formation of a carbon shell around silver nanoparticles, which traps conduction electrons. The charge dynamic variation in time at the particle–matrix interface causes the electron concentration in the particle to fluctuate. Fluctuation influences directly to the SPR relaxation. The lifetime of excited conduction electrons in the particle defines the SPR spectral width. Here, the contribution from electron scattering by the interface (because of restrictions imposed on the electron free path [4]) adds up with the charge dynamic variation at the interface. Thus, the temporal capture of conduction electrons from the particle broadens the SPR-related extinction spectra. Such effect was demonstrated with silver nanoparticles embedded in the C_{60} matrix [208]. Silver nanoparticles in the carbon matrix exhibit the much broader SPR band than in free space. We may therefore suppose that, as the dose rises, the charge dynamic redistribution may broaden the SPR spectra of silver nanoparticles synthesized by ion implantation in PMMA. This is because implantation carbonizes the irradiated layer with increasing absorbed dose and raises the amount of acceptor levels on the MNP surface, which change the relaxation time of electrons excited.

ACKNOWLEDGEMENTS

I wish to thank my partners and co-authors form different countries D. Hole, P.D. Townsend, I.B. Khaibullin, V.I. Nugdin, V.F. Valeev, V.N. Bazarov, Yu.N. Osin, S.N. Abdullin, V.A. Zikharev, I.A. Faizrakhmanov, V.N. Popok, and U. Kreibig, Also, I grateful to the Alexander von Humboldt Foundation and DAAD in Germany, Austrian Scientific Foundation in the frame of Lisa Meitner Fellowship and the Royal Society in UK for financial support. Partly, this work was supported by the Ministry of Education ans Science of the Russian Federation (FTP "Scientific and scientific-pedagogical personnel of the innovative Russia" contract №. 02.740.11.0779).

REFERENCES

[1] J. Z. Zhang, *Optical properties and spectroscopy of nanomaterials* (Wold Sci. Pub.: London, 2009).

[2] *Optical properties of nanostructured random media*, ed. by V.M. Shalaev (Springer: Berlin, 2002).

[3] C. Flytzanis, F. Hache, M.C. Klein, D. Ricard and P. Rousignol, *Nonlinear optics in composite materials* (Elsevier Science, Amsterdam, 1991).

[4] U. Kreibig and M. Vollmer, *Optical properties of metal clusters* (Springer, Berlin, 1995).

[5] A.L. Stepanov, I.B. Khaibullin, P.D. Townsend, Hole and A.A. Bukharaev, *RF Patent,* 2156490 (2000).

[6] P.D. Townsend and L. Massarelli, *US Patent* 5102736 (1992).

[7] J.M. Hampikian and E.M. Hunt, *US Patent*, 6294223 (2001).

[8] N. Kishimoto, Y. Takeda and S. Okubo, *Jap. Patent*, JP2004091817 (2004).

[9] P.T. Townsend, P.J. Chandler and L. Zhang, *Optical Effects of Ion Implantation* (Cambridge Univ. Press: Cambridge, 1994).

[10] A.L. Stepanov, In: *High-power and Femtosecond Lasers*, ed. by P.-H. Barret, P.-H. and M. Palmer (NOVA Sci. Publ. Inc.: New York, 2009), p. 27.

[11] J. Davenas, A. Perez, P. Thevenard and C.H.S. Dupuy // *Phys. Stat. Sol. A* **19** (1973) 679.

[12] M. Treilleux, P. Thevenard, G. Ghassagne and L.H. Hobbs // *Phys. Stat. Sol. A* **48** (1978) 425.

[13] G.W. Arnold // *J. Appl. Phys*. **46** (1975) 4466.

[14] G.W. Arnold and J.A. Borders // *J. Appl. Phys*. **48** (1977) 1488.

[15] A.L. Stepanov, In: *Metal-Polymer Nanocomposites*, ed. L. Nicolais and G. Carotenuto (John Wiley & Sons Publ: London, 2004) p. 241.

[16] F. Gonella and P. Mazzoldi, In: *Hand book of nanostructured materials and nanotechnology*, ed. by H.S. Nalwa (Academic Press, 2000).

[17] M. Rahmani, L.H. Abu-Hassan, P.D. Townsend, I.H. Wilson and G.L. Destefanis // *Nucl. Inst. Meth. Phys. Res. B* **32** (1988) 56.

[18] M. Rahmani and P.D. Townsend // *Vacuum* **39** (1989) 1157.

[19] C.W. White, D.K. Thomas, D.K. Hensley, J.C. McCallum, A. Pogany, R.F. Haglund Jr., R.H. Magruder and L. Yang // *Nanostruc. Mat.* **3** (1993) 447.

[20] D. Ila, E.K. Williams, S. Sarkisov, D.B. Poker and D.K. Hensley // *Mat. Res. Soc. Symp. Proc.* **504** (1998) 381.

[21] G. Steiner, M.T. Pham, Ch. Kuhne and R. Salzer // *Fresenius J Anal Chem*. **362** (1998) 9.

[22] R.A. Ganeev, A.I. Ryasnyanskii, A.L. Stepanov, C. Marques, R.C. da Silva and E. Alves // *Opt. Comm*. **253** (2005) 205.

[23] R.A. Ganeev, A.I. Ryasnyanskii, A.L. Stepanov, T. Usmanov, C. Marques, R.C. da Silva and E. Alves E. // *Optics and Spectroscopy* **101** (2006) 615.

[24] C. Marques, R.C. da Silva, A. Wemans, M.J.P. Maneira, A. Kozanecki and E. Alves // *Nucl. Inst. Meth. Phys. Res*. B **242** (2006) 104.

[25] P. Mazzoldi, I. Tramontin, A. Boscolo-Boscoletto, G. Battaglin and G.W. Arnold // *Nucl. Inst. Meth. Phys. Res. B* **80-81** (1993) 1192.

[26] G. Abouchacra and J. Serughetti // *Nucl. Inst. Meth. Phys. Res. B* **14** (1986) 282.

[27] G. Fuchs, G. Abouchacra, M. Treilleux, P. Thevenard and J. Serughetti // *Nucl. Inst. Meth. Phys. Res. B* **32** (1988) 100.

[28] Y. Qian, D. Ila, R.L. Zimmerman, D.B. Poker, L.A. Boatner and D.K. Hensley // *Nucl. Inst. Meth. Phys. Res. B* **127** (1997) 524.

[29] R.L. Zimmerman, C.I. Muntele and D. Ila // *Surf. Coat. Technol*. **196** (2005) 85.

[30] M.A. van Huis, A.V. Fedorov, A. van Veen, C.V. Falub, S.W.H. Eijt, B.J. Kooi, J.Th.M. De Hosson, T. Hibma and R.L. Zimmerman //

Nucl. Inst. Meth. Phys. Res. B **191** (2002) 442.
[31] X.H. Xiao, J.X. Xu, F. Ren, C. Liu and C.Z. Jiang // *Physica E* **40** (2008) 705.
[32] N. Matsunami and H. Hosono // *Nucl. Inst. Meth. Phys. Res. B* **80** (1993) 1233.
[33] S. Deying, Y. Saito and S. Suganomata // *Jpn. J. Appl. Phys*. **33** (1994) L966.
[34] D.Y. Shang, Y. Saito, Y.R. Kittaka, S. Taniguchi and A. Kitahara // *J. Appl. Phys.* **80** (1996) 6651.
[35] Y. Saito and A. Kitahara // *J. Appl. Phys.* **87** (2000) 1276.
[36] T. Fujita, K. Ijima, N. Mitsui, K. Mochiduki, A. Ho and Y. Saito // *Jap. J. Appl. Phys.* **47** (2008) 7224.
[37] S.S. Sarkisov, E.K. Williams, M.J. Curley, C.C. Smith, D. Ila, P. Venkateswarlu, D.B. Poker and D.K. Hensley // *Mat. Res. Soc. Symp. Proc.* **504** (1998) 357.
[38] S.S. Sarkisov, E.K. Williams, M.J. Curley, D. Ila, P. Venkateswarlu, D.B. Poker and D.K. Hensley // *Nucl. Inst. Meth. Phys. Res. B* **141** (1998) 294.
[39] S.S. Sarkisov, E.K. Williams, M.J. Curley, C.C. Smith, D. Ila, D.B. Poker, D.K. Hensley, C. Banks and B. Penn // *Proc. SPIE*. **3283** (1998) 942.
[40] S.S. Sarkisov, E.K. Williams, M.J. Curley, D. Ila, V.L. Svetchnikov, V.M. Pan, D.B. Poker, D.K. Hensley, C. Banks, B. Penn and J.W. Wang // *Proc. SPIE*. **3413** (1998) 98.
[41] S.S. Sarkisov, M.J. Curley, E.K. Williams, D. Ila, V.L. Svetchnikov, H.W. Zandbergen, G.A. Zykov, D.B. Poker and D.K. Hensley // *Proc. SPIE.* **3790** (1999) 43.
[42] S.S. Sarkisov, M.J. Curley, E.K. Williams, D. Ila, V.L. Svetchnikov, H.W. Zandbergen, G.A. Zykov, C. Banks, J.-C. Wang, D.B. Poker and D.K. Hensley // *Nucl. Inst. Meth. Phys. Res. B* **166-167** (2000) 750.
[43] E.K. Williams, D. Ila, S.S. Sarkisov, M.J. Curley, D.B. Poker, D.K. Hensley and C. Borel // *Mat. Res. Soc. Symp. Proc*. **504** (1998) 363.
[44] E.K. Williams, D. Ila, S.S. Sarkisov, M.J. Curley, J.C. Cochrane, D.B. Poker D.K. Hensley and C. Borel // *Nucl. Inst. Meth. Phys. Res. B* **141** (1998) 268.
[45] E.K. Williams, D. Ila, A. Darwish, D.B. Poker, S.S. Sarkisov, M.J. Curley, J.-C. Wang, V.L. Svetchnikov and H.W. Zandbergen // *Nucl. Inst. Meth. Phys. Res. B* **148** (1999) 1074.
[46] G.O. Amolo, J.D. Comins, S.R. Naidoo, S.H. Connell, M.J. Witcomb and T.E. Derry // *Nucl. Inst. Meth. Phys. Res. B* **250** (1999) 233.
[47] P. Mazzoldi, L. Tramontin, A. Boscolo-Boscoletto, G. Battaglin and G.W. Arnold // *Nucl. Inst. Meth. Phys. Res. B* **80-81** (1993) 233.
[48] P. Mazzoldi and G. Mattei // *Rivista del nuovo cimento* **28** (2005) 1.
[49] P. Mazzoldi and G. Mattei // *Phys. Stat. Sol. A* **204** (2007) 621.
[50] M. Antonello, G.W. Arnold, G. Battaglin, R. Bertoncello, E. Cattaruzza, P. Colombo, G. Mattei, P. Mazzoldi, and F. Trivillin // *J. Mater. Chem.* **8** (1998) 457.
[51] G. Battaglin, E. Cattaruzza, F. D'Acapito, F. Gonella, P. Mazzoldi, S. Mobilio F. Priolo // *Nucl. Inst. Meth. Phys. Res. B* **141** (1998) 252.
[52] G. Battaglin, M. Catalano, E. Cattaruzza, F. D'Acapito, C. De Julian Fernandez, G. De Marchi, F. Gonella, G. Mattei, C. Maurizio, P. Mazzoldi, A. Miotello and C. Sada // *Nucl. Inst. Meth. Phys. Res. B* **178** (2001) 176.
[53] R. Bertoncello, S. Gross, F. Trivillin, E. Cattaruzza, G. Mattei, F. Caccavale, P. Mazzoldi and G. Battaglin // *J. Mater. Res.* **14** (1999) 2449.
[54] F. Caccavale // *Pramana - J. Phys*. **50** (1998) 653.
[55] E. Cattaruzza, G. Battaglin, R. Polloni, T. Cesca, F. Gonella, G. Mattei, C. Maurizio, P. Mazzoldi, F. D'Acapito, F. Zontone and R. Bertoncello // *Nucl. Inst. Meth. Phys. Res. B* **148** (1990) 1007.
[56] F. Gonella, G. Mattei, P. Mazzoldi, C. Sada, G. Battaglin and E. Cattaruzza // *Appl. Phys. Lett*. **75** (1999) 55.
[57] N. Matsunami and H. Hosono // *Appl. Phys. Lett*. **63** (1993) 2050.
[58] R.H. Magruder III, R.A. Zuhr and D.H. Osborne, Jr. // *Nucl. Inst. Meth. Phys. Res. B* **99** (1995) 590.
[59] R.H. Magruder III, T.S. Anderson, R.A. Zuhr and D.K. Thomas // *Nucl. Inst. Meth. Phys. Res. B* **108** (1996) 305.
[60] R.H. Magruder III, S.J. Robinson, C. Smith, A. Meldrum, A. Halabica and R.H. Haglund, Jr. // *J. Appl. Phys*. **105** (2009) 24303.
[61] T.S. Anderson, R.H. Magruder III, R.A. Zuhr and J.E. Wittig // *J. Electronic Mater.* **25** (1996) 27.

[62] T.S. Anderson, R.H. Magruder III, D.L. Kinser, R.A. Zuhr and D.K. Thomas // *Nucl. Inst. Meth. Phys. Res. B* **124** (1997) 40.
[63] T.S. Anderson, R.H. Magruder III, D.L. Kinser, J.E. Wittig, R.A. Zuhr and D.K. Thomas // *J. Non.-Cryst. Sol*. **224** (1998) 299.
[64] T.S. Anderson, R.H. Magruder III, J.E. Wittig, D.L. Kinser and R.A. Zuhr // *Nucl. Inst. Meth. Phys. Res. B* **171** (2000) 401.
[65] R.A. Zuhr, R. H. Magruder III and T.S. Anderson // *Surf. Coat. Technol*. **101** (1998) 401.
[66] M.T. Pham, W. Matz and H. Seifarth // *Anal. Chim. Acta* **350** (1997) 209.
[67] Z. Liu, H. Wang, H. Li and X. Wang // *Appl. Phys. Lett*. **72** (1998) 1823.
[68] Z. Liu, H. Li, X. Feng, S. Ren, Z. Liu and B. Lu // *J. Appl. Phys*. **84** (1998) 1913.
[69] Z. Liu, H. Li, H. Wang, D. Shen, X. Wang and P.F.A. Alkemade // *J. Mater. Res*. **15** (2000) 1245.
[70] D. Ila, E.K. Williams, S. Sarkisov, C.C. Smith, D.B. Poker and D.K. Hensley // *Nucl. Inst. Meth. Phys. Res*. *B* **141** (1998) 289.
[71] F. D'Acapito and F. Zontone // *J. Appl. Cryst.* **32** (1999) 234.
[72] A.L. Stepanov, D.E. Hole and P.D. Townsend // *Nucl. Inst. Meth. Phys. Res. B* **166-167** (2000) 882.
[73] A.L. Stepanov // *Rev. Adv. Mater. Sci.* **4** (2003) 45.
[74] C.Z. Jiang and X.J. Fan // *Surf. Coat. Technol*. **131** (2000) 330.
[75] F. Ren, C.Z. Jiang, H.B. Chen, Y. Shi, C. Liu and J.B. Wang // *Physics B* **353** (2004) 92.
[76] F. Ren, C.Z. Jiang, L. Zhang, Y. Shi, J.B. Wang and R.H. Wang // *Micron* **35** (2004) 489.
[77] F. Ren, C.Z. Jiang, C. Liu and Y. Shi // *J. Kor. Phys. Soc*. **46** (2005) S43.
[78] F. Ren, C.Z. Jiang, D.J. Fu and Q. Ru // *Jap. J. Appl. Phys*. **44** (2005) 8512.
[79] F. Ren, C.Z. Jiang, C. Liu, D. Fu and Y. Shi // *Solid State Comm*. **135** (2005) 268.
[80] F. Ren, C.Z. Jiang, C. Liu, J. Wang and T. Oku // *Phys. Rev. Lett*. **97** (2006) 165501.
[81] F. Ren, C.Z. Jiang, G.X. Cai, Q. Fu and Y. Shi // *Nucl. Inst. Meth. Phys. Res. B* **262** (2007) 201.
[82] F. Ren, G.X. Cai, X.H. Xiao, L.X. Fan, C. Liu, D.J. Fu, J.B. Wang and C.Z. Jiang // *J. Appl. Phys*. **103** (2008) 843308.
[83] F. Ren, X.H. Xiao, G.X. Cai, J.B. Wang and C.Z. Jiang // *Appl. Phys. A* **96** (2009) 317.
[84] X.F. Liu, C.Z. Jiang, R. Feng and Q. Fu // *Acta Phys. Sinca* **54** (2005) 4633.
[85] X.H. Xiao, C.Z. Jiang, F. Ren, J. Wang and Y. Shi // *Solid State Comm*. **137** (2006) 362.
[86] X.H. Xiao, F. Ren, J.B. Wang, C. Liu and C.Z. Jiang // *Mater. Lett.* **61** (2007) 4435.
[87] X.H. Xiao, L.P. Guo, F. Ren, J.B. Wang, D.J. Fu, D.L. Chen, Z.Y. Wu, Q.J. Jia, C. Liu and C.Z. Jang // *Appl. Phys. A* **89** (2007) 681.
[88] Y.H. Wang, C.Z. Jiang, F. Ren, Q.Q. Wang, D.J. Chen and D.J. Fu // *J. Mater. Sci.* **42** (2007) 7294.
[89] Y.H. Wang, C.Z. Jiang, X.H. Xiao and D.J. Chen // *Physica B* **403** (2008) 2143.
[90] L. Zhang, C.Z. Jiang, F. Ren, H.-B. Chen, Y. Shi and Q. Fu // *Acta Phys. Sinica* **53** (2004) 2910.
[91] G.X. Cai, F. Ren, X.H. Xiao, L.X. Fan and C.Z. Jiang // *Nucl. Inst. Meth. Phys*. Res. B **266** (2008) 889.
[92] G.X. Cai, F. Ren, X.H. Xiao, L.X. Fan, X.D. Zhou and C.Z. Jiang // *J. Mater. Sci. Technol.* **25** (2009) 669.
[93] L. Armelao, R. Bertoncello, E. Cattaruzza, S. Gialanella, S. Gross, G. Mattei, P. Mazzoldi and E.J. Tondello // *Mater. Chem*. **12** (2002) 2401.
[94] J. Ishikawa, H. Tsuji, M. Motono, Y. Gotoh, N. Arai, K. Adachi and H. Kotaki // *IEEE* **12** (2002) 690.
[95] J. Ishikawa, H. Tsuji, M. Motono and Y. Gotoh // *Surf. Coat. Technol*. **203** (2009) 2351.
[96] H. Tsuji, K. Kurita, Y. Gotoh, N. Kishimoto and J. Ishikawa // *Nucl. Inst. Meth. Phys. Res. B* **192** (2002) 315.
[97] H. Tsuji, K. Kurita and M. Motono // *J. Vac. Soc. Jap*. **45** (2002) 528.
[98] H. Tsuji, N. Arai, M. Motono, Y. Gotoh, K. Abachi, H. Kotaki and J. Ishikawa // *Nucl. Inst. Meth. Phys. Res. B* **206** (2003) 615.
[99] H. Tsuji, N. Arai, T. Matsumoto, K. Ueno, Y. Gotoh, K. Abachi, H. Kotaki and J. Ishikawa // *Appl. Surf. Sci*. **238** (2004) 132.
[100] H. Tsuji, N. Arai, T. Matsumoto, K. Ueno, K. Abachi, H. Kotaki, Y. Gotoh and J. Ishikawa // *Surf. Coat. Technol*. **196** (2005) 39.
[101] N. Arai, H. Tsuji, M. Motono, Y. Goto, K. Adachi, H. Kotaki and J. Ishikawa // *Nucl. Inst. Meth. Phys. Res. B* **206** (2003) 629.

[102] N. Arai, H. Tsuji, K. Ueno, T. Matsumoto, Y. Gotoh, K. Abachi, H. Kotaki and J. Ishikawa // *Surf. Coat. Technol*. **196** (2005) 44.
[103] N. Arai, H. Tsuji, K. Ueno, T. Matsumoto, Y. Gotoh, K. Abachi, H. Kotaki, Y. Gotoh and J. Ishikawa // *Nucl. Inst. Meth. Phys. Res. B* **242** (2006) 217.
[104] N. Arai, H. Tsuji, K. Abachi, H. Kotaki, Y. Gotoh and J. Ishikawa // *Jap. J. Appl. Phys.* **46** (2007) 6260.
[105] N. Arai, H. Tsuji, N. Gotoh, T. Matsumoto, T. Ishibashi, K. Adachi, H. Kotaki, Y. Gotoh and J. Ishikawa // *J. Phys.: Conf. Ser*. **61** (2007) 41.
[106] J. Roiz, A. Oliver, E. Munoz, L. Rodríguez-Fernández, J.M. Hernandez, J. C. Cheang-Wong // *J. App. Phys.* **95** (2004) 1783.
[107] A. Oliver, J.A. Reyes-Esqueda, J.C. Cheang-Wong, J.E. Román-Velázquez, A. Crespo-Sosa, L. Rodríguez-Fernández, J.A. Seman and C. Noguez // *Phys. Rev. B* **74** (2006) 245425.
[108] J.C. Cheang-Wong, A. Oliver, L. Rodríguez-Fernández, J. Arenas-Alatorre, O. Peña and A. Crespo-Sosa // *Revista Mexicana de Física S* **53** (2007) 49.
[109] O. Peña, J.C. Cheang-Wong, L. Rodríguez-Fernández, J. Arenas-Alatorre, A. Crespo-Sosa, V. Rodríguez –Iglesias and A. Oliver // *Nucl. Inst. Meth. Phys. Res. B* **257** (2007) 99.
[110] O. Peña, U. Pal, L. Rodríguez-Fernández, H.G. Silva-Pereyra, V. Rodríguez -Iglesias, J.C. Cheang-Wong, J. Arenas-Alatorre and A. Oliver // *J. Phys. Chem.* **113** (2009) 2296.
[111] J.A. Reyes-Esqueda, C. Torres-Torres, J.C. Cheang-Wong, A. Crespo-Sosa, L. Rodríguez-Fernández, C. Noguez and A. Oliver // *Opt. Express* **16** (2008) 710.
[112] J.A. Reyes-Esqueda, V. Rodríguez -Iglesias, H.G. Silva-Pereyra, C. Torres-Torres, A.-L. Santiago-Ramirez, J.C. Cheang-Wong, A. Crespo-Sosa, L. Rodríguez-Fernández, A. Lopez-Suarez and A. Oliver // *Opt. Express* **17** (2009) 12849.
[113] V. Rodríguez -Iglesias, H.G. Silva-Pereyra, J.C. Cheang-Wong, J.A. Reyes-Esqueda, L. Rodríguez-Fernández, A. Crespo-Sosa, G. Kellerman and A. Oliver // *Nucl. Inst. Meth. Phys. Res. B* **266** (2008) 3138.
[114] V. Rodríguez -Iglesias, H.G. Silva-Pereyra, C. Torres-Torres, J.A. Reyes-Esqueda, J.C. Cheang-Wong, A. Crespo-Sosa, L. Rodríguez-Fernández, A. López-Suárez, and A. Oliver // *Opt. Comm*. **282** (2009) 4157.
[115] R. Rangel-Rojo, J. McCarthy, H.T. Bookey, A.K. Kar, L. Rodríguez-Fernández, J.C. Cheang-Wong, A. Crespo-Sosa, A. Lopez-Sosa, A. Oliver, V. Rodríguez –Iglesias and H.G. Silva-Pereyra // *Opt. Comm*. **282** (2009) 1909.
[116] A. Romanyuk, V. Spassov and V.J. Melnik // *Appl. Phys*. **99** (2006) 034314.
[117] Y. Takeda, O.A. Plaksin, J. Lu and N. Kishimoto // *Vacuum* **80** (2006) 776.
[118] B. Joseph, C.S. Suchan Sandeep, B.R. Sekhar, D.P. Mahapatra and R. Philip // *Nucl. Inst. Meth. Phys. Res. B* **265** (2007) 631.
[119] B. Joseph, H.P. Lenka, P.K. Kuiri, D.P. Mahapatra and R. Kesavamoorthy // *Intern. J. Nanoscience* **6** (2007) 423.
[120] G. Sahu, S.K. Rath, B. Joseph, G.S. Roy and D.P. Mahapatra // *Vacuum* **83** (2009) 836.
[121] R. Carles, C. Farcău, C. Bonafos, G. Benassayag, B. Pécassou and A. Zwick // *Nanotechnol.* **20** (2009) 1.
[122] Y.H. Wang, S.J. Peng, J.D. Lu, R.W. Wang, Y.I. Mao and Y.G. Chen // *Vacuum* **83** (2009) 408.
[123] Y.H. Wang, S.J. Peng, J.D. Lu, R.W. Wang, Y.G. Chen and Y.I. Mao // *Vacuum* **83** (2009) 412.
[124] R.H. Magruder III and A. Meldrum // *J. Non.-Cryst. Solids* **353** (2007) 4813.
[125] L.C. Nistor, J. von Landuyt, J.B. Barton, D.E. Hole, N.D. Skelland and P.D. Townsend // *Non.-Cryst. Solids* **162** (1993) 217.
[126] R.A. Wood, P.D. Townsend, N.D. Skelland, D.E. Hole, J. Barton and C.N. Afonso // *J. Appl. Phys*. **74** (1993) 5754.
[127] M. Dubiel, H. Hofmeister and E. Schurig // *Phys. Stat. Sol. B* **203** (1997) R5.
[128] M. Dubiel, H. Hofmeister, E. Schurig, E. Wendler and W. Wesch // *Nucl. Inst. Meth. Phys. Res. B* **166-167** (2000) 871.
[129] M. Dubiel, H. Hofmeister, G.L. Tan, K.-D. Schicke and E. Wendler // *Eur. Phys. J. D* **24** (2003) 361.
[130] M. Dubiel, H. Hofmeister and E. Wendler // *J. Non.-Cryst. Solids* **354** (2008) 607.
[131] G. Seifert, S. Stalmashonak, H. Hofmeister, J. Haug and M. Dubiel // *Nanoscale Res. Lett.* **4** (2009) 1380.

[132] A.L. Stepanov, D.E. Hole, A.A. Bukharaev, P.D. Townsend and N.I. Nurgazizov // *Appl. Surf. Sci.* **136** (1998) 298.
[133] A.L. Stepanov, D.E. Hole and P.D. Townsend // *J. Non.-Cryst. Solids* **224** (1999) 275.
[134] A.L. Stepanov, D.E. Hole and P.D. Townsend // *J. Non.-Cryst. Solids* **260** (1999) 67.
[135] A.L. Stepanov, D.E. Hole and P.D. Townsend // *Nucl. Inst. Meth. Phys. Res. B* **149** (1999) 89.
[136] A.L. Stepanov, D.E. Hole and P.D. Townsend // *Nucl. Inst. Meth. Phys. Res. B* **161-163** (2000) 913.
[137] A.L. Stepanov, V.A. Zhikharev, D.E. Hole, P.D. Townsend and I.B. Khaibullin // *Nucl. Inst. Meth. Phys. Res. B* **166-167** (2000) 26.
[138] A.L. Stepanov, D.E. Hole and P.D. Townsend // *Nucl. Inst. Meth. Phys. Res. B* **166-167** (2000) 882.
[139] A.L. Stepanov // *Optics and Spectroscopy* **89** (2000) 408.
[140] A.L. Stepanov, V.N. Popok, D.E. Hole and A.A. Bukharaev // *Physics of Solid State* **43** (2001) 2192.
[141] A.L. Stepanov and V.N. Popok // *J. Appl. Spectr*. **68** (2001) 164.
[142] A.L. Stepanov, D.E. Hole and V.N. Popok // *Tech. Phys. Lett*. **27** (2001) 554.
[143] A.L. Stepanov, D.E. Hole and A.A. Bukharaev // *Vacuum* **64** (2002) 169.
[144] A.L. Stepanov, D.E. Hole and V.N. Popok // *Glass Phys. Chem*. **28** (2002) 90.
[145] A.L. Stepanov and D.E. Hole // *Phil. Mag. Lett*. **82** (2002) 149.
[146] A.L. Stepanov, *Recent research development in applied physics, edited by S.G. Pandalai* (Transworld Res. Network: Kerala, 2002), vol. 5, p. 1.
[147] A.L. Stepanov and V.N. Popok // *Tech. Phys. Lette*. **29** (2003) 977.
[148] A.L. Stepanov // *Rev. Adv. Mater. Sci* **4** (2003) 45.
[149] A.L. Stepanov, In: *Recent research development in non.-crystalline solids*, ed. by S.G. Pandalai S. G. (Transworld Res. Network: Kerala, 2003), vol. 3, p. 177.
[150] A.L. Stepanov and V.N. Popok // *Surf. Coat. Thechnol*. **185** (2004) 30.
[151] A.L. Stepanov and V.N. Popok // *Surf. Sci*. **566-568** (2004) 1250.
[152] A.L. Stepanov and V.N. Popok // *J. Appl. Spectr*. **72** (2005) 229.
[153] A.L. Stepanov, B.N. Chichkov, V.F. Valeev and I.A. Faizrakhmanov // *Tech. Phys. Lett*. **34** (2008) 184.
[154] A.L. Stepanov, V.F. Valeev, I.A. Faizrakhmanov and B.N. Chichkov // *Tech. Phys. Lett.* **34** (2008) 1014.
[155] A.L. Stepanov, V.F. Valeev, V.V. Bazarov and I.A. Faizrakhmanov // *Tech. Phys*. **54** (2009) 1504.
[156] H. Tsuji, H. Sugahara, Y. Gotoh and J. Ishikawa // *Surf. Coat. Thechnol*. **158-159** (2002) 208.
[157] H. Tsuji, H. Sugahara, Y. Gotoh and J. Ishikawa // *Nucl. Inst. Meth. Phys. Res. B* **206** (2003) 249.
[158] H. Tsuji, N. Sakai, H. Sugahara, Y. Gotoh and J. Ishikawa // *Nucl. Inst. Meth. Phys. Res. B* **237** (2005) 433.
[159] H. Tsuji, N. Sakai, Y. Gotoh and J. Ishikawa // *Nucl. Inst. Meth. Phys. Res. B* **242** (2006) 129.
[160] Y. Saito, Y. Imamura and A. Kitahara // *Nucl. Inst. Meth. Phys. Res. B* **205** (2003) 272.
[161] T. Fujita, K. Ijima, N. Mitsui, K. Mochiduki and Y. Saito // *Jap. J. Appl. Phys*. **46** (2007) 7362.
[162] J.F. Ziegler, J.P. Biersack and U. Littmark, *The stopping and range of ions in solids* (Pergamon Press: New York, 1996).
[163] M. Nastasi, J.W. Mayer and J.K. Hiroven, *Ion-solid interactions: Fundamentals and applications* (Cambridge Univ. Press: Cambridge, 1996).
[164] S. Namba, K. Masuda, K. Gamo, A. Doi, S. Ishinara and I. Kimura, In: *Ion implantation. Proc. Of conf. on ion implantation in semiconductors*, ed. by F.D. Eisen and L.T. Chadderton (Cordon and Breach Sci. Publ.: London, 1971), p. 231.
[165] A. Berger // *J. Non.-Cryst. Solids* **151** (1992) 88.
[166] N.D. Skelland and P.D. Townsend // *J. Non.-Cryst. Solids* **188** (1995) 243.
[167] D.E. Hole, A.L. Stepanov and P.D. Townsend // *Nucl. Inst. Meth. Phys. Res. B* **148** (1999) 1054.
[168] V.M. Konoplev // *Radiat. Eff. Lett*. **87** (1986) 207.
[169] V.M. Konoplev, M. Vicanek and A. Gras-Martí // *Nucl. Inst. Meth. Phys. Res. B* **67** (1992) 574.
[170] A.L. Stepanov, S.N. Abdullin, R.I. Khaibullin, V.F. Valeev, Yu.N. Osin, V.V. Bazarov and

I.B. Khaibullin // *Mat. Res. Soc. Proc*. **392** (1995) 267.
[171] R.I. Khaibullin, Yu.N. Osin, A.L. Stepanov and I.B. Khaibullin // *Nucl. Inst. Meth. Phys. Res. B* **148** (1999) 1023.
[172] P.D. Townsend, N. Can, P.J. Chandler, B.W. Farmery, R. Lopez-Heredero, A. Peto, L. Salvin, D. Underdown and B.J. Yang // *Non.-Cryst. Solids* **223** (1998) 73.
[173] P.W. Wang // *Appl. Surf. Sci*. **120** (1997) 291.
[174] J. Bartels, U. Lembke, R. Pascova, J. Schmelzer and I.J. Gustzow // *Non.-Cryst. Solids* **136** (1991) 181.
[175] G. Mie // *Ann. Phys*. **25** (1908) 377.
[176] O.S. Heavens, *Optical properties of thin solid films, Butterworths* (Sci. Pub.: London, 1955).
[177] J.C. Maxwell Garnet // *Philos. Trans. R. Soc. Lond*. **203** (1904) 385.
[178] J.C. Maxwell Garnet // *Philos. Trans. R. Soc. Lond*. **205** (1906) 237.
[179] A. Faik, L. Allen, C. Eicher, A. Gagola, P.D. Townsend and C.W. Pitt // *J. Appl. Phys.* **54** (1983) 2597.
[180] H. Hosono // *Jpn. J. Appl. Phys*. **32** (1993) 3892.
[181] A.L. Stepanov, V.F. Valeev, Yu.N. Osin, Yu. V.I. Nuzhdin and I.A. Faizrakhmanov // *Tech. Phys*. **54** (2009) 997.
[182] A. Heilmann, *Polymer films with embedded metal nanoparticles* (Springer: Berlin, 2003).
[183] N.C. Koon, D. Weber, P. Pehrsson and A.I. Sindler // *Mater. Res. Soc. Proc.* **27** (1984) 445.
[184] A.L. Stepanov, S.N. Abdullin, R.I. Khaibullin, Yu.N. Osin and I.B. Khaibullin // *Proc. Royal Micr. Sci.* **29** (1994) 226.
[185] A.L. Stepanov, S.N. Abdullin, R.I. Khaibullin, V.F. Valeev, Yu.N. Osin, V.V. Bazarov and I.B. Khaibullin // *Mat. Res. Soc. Proc*. **392** (1995) 267.
[186] A.L. Stepanov, S.N. Abdullin, R.I. Khaibullin and I.B. Khaibullin, *RF Patent*, 109708, 1997.
[187] A.L. Stepanov, R.I. Khaibullin, V.F. Valeev, Yu.N. Osin, V.I. Nuzhdin and I.F. Faizrakhmanov // *Tech. Phys*. **54** (2009) 1162.
[188] I.B. Khaibullin, R.I. Khaibullin, S.N. Abdullin, A.L. Stepanov, Yu.N. Osin, V.V. Bazarov and S.P. Kurzin // *Nucl. Inst. Meth. Phys. Res. B* **127-128** (1997) 685.
[189] H. Boldyryeva, N. Kishimoto, N. Umeda, K. Kono, O.A. Plaksin and Y. Takeda // *Nucl. Inst. Meth. Phys. Res. B* **219-220** (2004) 953.
[190] Y. Wu, T. Zhang, H. Zhang, X. Zhang, Z. Deng and G. Zhou // *Nucl. Inst. Meth. Phys. Res. B* **169** (2000) 89.
[191] Y. Wu, T. Zhang, Y. Zhang, H. Zhang, X. Zhang and G. Zhou // *Nucl. Inst. Meth. Phys. Res. B* **173** (2001) 292.
[192] Y. Wu, T. Zhang, Y. Zhang, H. Zhang, X. Zhang and G. Zhou // *Science in China E* **44** (2001) 493.
[193] Y. Wu, T. Zhang, A. Liu and G. Zhou // *Surf. Coat. Technol*. **157** (2002) 262.
[194] T. Kobayashi, T. Iwata, Y. Doi and M. Iwaki // *Nucl. Inst. Meth. Phys. Res. B* **175-177** (2001) 548.
[195] A.L. Stepanov, S.N. Abdullin, V.Yu. Petukhov, Yu.N. Osin, R.I. Khaibullin and I.B. Khaibullin // *Phil. Mag. B* **80** (2000) 23.
[196] A.L. Stepanov, V.N. Popok, I.B. Khaibullin and U. Kreibig // *Nucl. Inst. Meth. Phys. Res. B* **191** (2002) 473.
[197] A.L. Stepanov // *Tech. Phys*. **49** (2004) 143.
[198] V.V. Bazarov, V.Yu. Petukhov, V.A. Zhikharev and I.B. Khaibullin // *Mater. Res. Soc. Proc.* **388** (1995) 417.
[199] H. Boldyryeva, N. Umeda, O.A. Plaksin, Y. Takeda and N. Kishimoto // *Surf. Coat. Thech*. **196** (2005) 373.
[200] R.I. Khaibullin, Y.N. Osin, A.L. Stepanov and I.B. Khaibullin // *Vacuum* **51** (1998) 289.
[201] R.I. Khaibullin, Yu.N. Osin, A.L. Stepanov and I.B. Khaibullin // *Nucl. Inst. Meth. Phys. Res. B* **148** (1999) 1023.
[202] A.L. Stepanov, R.I. Khaibullin and I.B. Khaibullin // *Phil. Mag. Lett*. **77** (1998) 261.
[203] W. Scheunemann and H. Jäger // *Z. Phys*. **265** (1973) 441.
[204] D.V. Sviridov // *Russian Chem. Rev*. **71** (2002) 315.
[205] B. Pignataro, M.E. Fragala and O. Puglisi // *Nucl. Instr. Meth. Phys. Res*. *B* **131** (1997) 141.
[206] J. Sinzig and M. Quinten // *Appl. Phys*. *A* **58** (1994) 157.
[207] U. Kreibig, M. Gartz and A. Hilger // *Ber. Bunssenges. Phys. Chem*. **101** (1997) 1593.
[208] J. Hölzl, F. Schulte and H. Wagner, *Solid surface physics* (Springer: Berlin, 1979).